1

MIMO RADAR — DIVERSITY MEANS SUPERIORITY

Jian Li

Department of Electrical and Computer Engineering, University of Florida, Gainesville

Petre Stoica

Information Technology Department, Uppsala University, Uppsala, Sweden

1.1 INTRODUCTION

MIMO radar is an emerging technology that is attracting the attention of researchers and practitioners alike. Unlike a standard phased-array radar, which transmits scaled versions of a single waveform, a MIMO radar system can transmit via its antennas multiple probing signals that may be chosen quite freely (see Fig. 1.1). This waveform diversity enables superior capabilities compared with a standard phased-array radar. In Refs. 1–4, for example, the diversity offered by widely separated transmit/receive antenna elements was exploited. Many other papers, including, for instance, Refs. 5–29, have considered the merits of a MIMO radar system with collocated antennas. The advantages of a MIMO radar system with both collocated and widely separated antenna elements are investigated in Ref. 30.

For collocated transmit and receive antennas, the MIMO radar paradigm has been shown to offer higher resolution (see, e.g., Refs. 6 and 9), higher sensitivity to detecting slowly moving targets [11], better parameter identifiability [15,18], and direct applicability of adaptive array techniques [15,26,27]. Waveform optimization has also been shown to be a unique capability of a MIMO radar system. For example, it has been used to achieve flexible transmit beampattern designs

MIMO Radar Signal Processing, edited by Jian Li and Petre Stoica

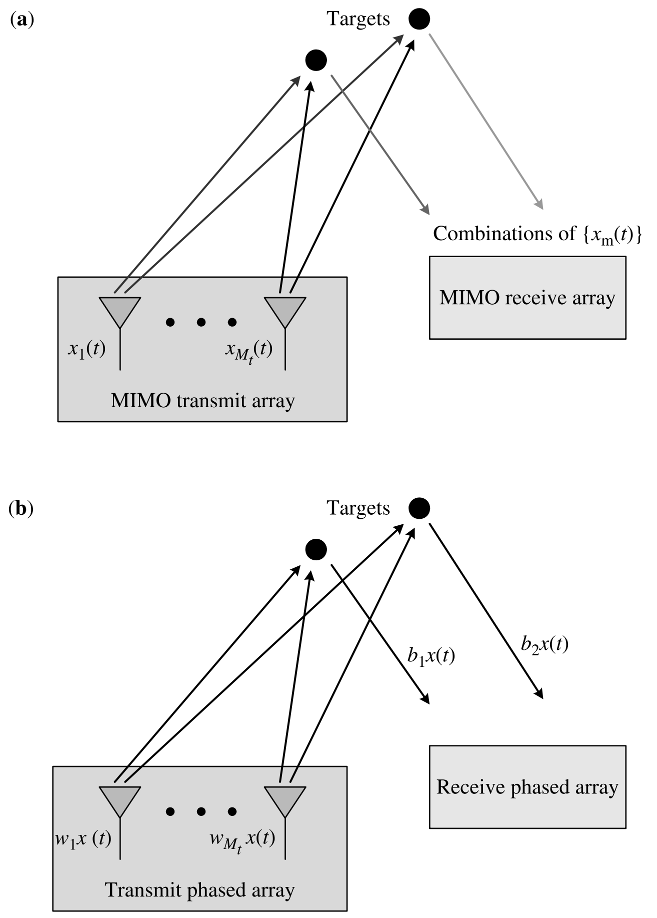

Figure 1.1 (a) MIMO radar versus (b) phased-array radar.

(see, e.g., Refs. 5, 12, 13, 17, and 23) as well as for MIMO radar imaging and parameter estimation [10,19,29].

In this chapter we present more recent results showing that this waveform diversity enables the MIMO radar superiority in several fundamental aspects. We focus on the case of collocated antennas. Without loss of generality, we consider targets associated with a particular range and Doppler bin. Targets in adjacent range bins can be viewed as interferences for the range bin of interest.

In Section 1.3 we address a basic aspect on MIMO radar — its parameter identifiability, which is the maximum number of targets that can be uniquely identified by the radar. We show that the waveform diversity afforded by MIMO radar enables a much improved parameter identifiability over its phased-array counterpart; specifically, the maximum number of targets that can be uniquely identified by the MIMO radar is up to M_t times that of its phased-array counterpart, where M_t is the number of transmit antennas. The parameter identifiability is further demonstrated in a numerical study using both the Cramér–Rao bound (CRB) and a least-squares method for target parameter estimation.

In Section 1.4 we consider nonparametric adaptive MIMO radar techniques that can be used to deal with multiple targets. Linearly independent waveforms can be transmitted simultaneously via the multiple transmit antennas of a MIMO radar. Because of the different phase shifts associated with the different propagation paths from the transmitting antennas to targets, these independent waveforms are linearly combined at the target locations with different phase factors. As a result, the signal waveforms reflected from different targets are linearly independent of each other, which allows for the direct application of Capon (after J. Capon) and of other adaptive array algorithms. In the absence of array steering vector errors, we discuss the application of several existing data-dependent beamforming algorithms, including Capon, APES (amplitude and phase estimation) and CAPES (combined Capon and APES), and then present an alternative estimation procedure, referred to as the *combined Capon–approximate maximum-likelihood* (CAML) method. In the presence of array steering vector errors, we apply the robust Capon beamformer (RCB) and doubly constrained robust Capon beamformer (DCRCB) approaches to the MIMO radar system to achieve accurate parameter estimation and superior interference and jamming suppression performance.

In Section 1.5 we discuss parametric methods for parameter estimation and number detection of MIMO radar targets. Cyclic optimization algorithms are presented to obtain the maximum-likelihood (ML) estimates of the target parameters, and a Bayesian information criterion (BIC) is used for target number detection. Specifically, an approximate cyclic optimization (ACO) approach is first presented, which maximizes the likelihood function approximately. Then an exact cyclic optimization (ECO) approach that maximizes the exact likelihood function is introduced for target parameter estimation. The ACO and ECO target parameter estimates are used with the BIC for target number determination.

In Section 1.6, we show that the probing signal vector transmitted by a MIMO radar system can be designed to approximate a desired transmit beampattern and also to minimize the cross-correlation of the signals bounced from various targets of interest — an operation that would hardly be possible for a phased-array radar. An efficient semidefinite quadratic programming (SQP) algorithm can be used to solve the signal design problem in polynomial time. Using this design, we can significantly improve the parameter estimation accuracy of the adaptive MIMO radar techniques. In addition, we consider a minimum sidelobe beampattern design. We demonstrate the advantages of these MIMO transmit beampattern designs over their phased-array counterparts. Because of the significantly larger number of degrees of freedom of a MIMO system, we can achieve much better transmit beampatterns with a MIMO radar, under the practical uniform elemental transmit power constraint, than with its phased-array counterpart. We also present an application of the MIMO transmit beampattern designs to the ultrasound hyperthermia treatment of breast cancer. By choosing a proper covariance matrix of the transmitted waveforms under the uniform elemental power constraint, the ultrasound system can provide a focal spot matched to the entire tumor region, and simultaneously minimize the impact on the surrounding healthy breast tissue.

1.2 PROBLEM FORMULATION

Consider a MIMO radar system with M_t transmit antennas and M_r receive antennas. Let $x_m(n)$ denote the discrete-time baseband signal transmitted by the mth transmit antenna. Also, let θ denote the location parameter(s) of a generic target, for example, its azimuth angle and its range. Then, under the assumption that the transmitted probing signals are narrowband and that the propagation is nondispersive, the baseband signal at the target location can be described by the expression (see, e.g., Refs. 12 and 17 and Chapter 6 in Ref. 31):

$$\sum_{m=1}^{M_t} e^{-j2\pi f_0 \tau_m(\theta)} x_m(n) \stackrel{\Delta}{=} \mathbf{a}^*(\theta)\mathbf{x}(n), \quad n = 1, \ldots, N \tag{1.1}$$

where f_0 is the carrier frequency of the radar, $\tau_m(\theta)$ is the time needed by the signal emitted via the mth transmit antenna to arrive at the target, $(\cdot)^*$ denotes the conjugate transpose, N denotes the number of samples of each transmitted signal pulse

$$\mathbf{x}(n) = [x_1(n) \quad x_2(n) \quad \cdots \quad x_{M_t}(n)]^T \tag{1.2}$$

and

$$\mathbf{a}(\theta) = \left[e^{j2\pi f_0 \tau_1(\theta)} \quad e^{j2\pi f_0 \tau_2(\theta)} \quad \cdots \quad e^{j2\pi f_0 \tau_{M_t}(\theta)}\right]^T \tag{1.3}$$

where $(\cdot)^T$ denotes the transpose. By assuming that the transmit array of the radar is calibrated, $\mathbf{a}(\theta)$ is a known function of θ.

Let $y_m(n)$ denote the signal received by the mth receive antenna; let

$$\mathbf{y}(n) = [y_1(n) \quad y_2(n) \quad \cdots \quad y_{M_r}(n)]^T, \quad n = 1, \ldots, N \tag{1.4}$$

and let

$$\mathbf{b}(\theta) = \left[e^{j2\pi f_0 \tilde{\tau}_1(\theta)} \quad e^{j2\pi f_0 \tilde{\tau}_2(\theta)} \quad \cdots \quad e^{j2\pi f_0 \tilde{\tau}_{M_r}(\theta)}\right]^T \tag{1.5}$$

where $\tilde{\tau}_m(\theta)$ is the time needed by the signal reflected by the target located at θ to arrive at the mth receive antenna. Then, under the simplifying assumption of point targets, the received data vector can be described by the equation (see, e.g., Refs. 3 and 28)

$$\mathbf{y}(n) = \sum_{k=1}^{K} \beta_k \mathbf{b}^c(\theta_k)\mathbf{a}^*(\theta_k)\mathbf{x}(n) + \boldsymbol{\epsilon}(n), \quad n = 1, \ldots, N \tag{1.6}$$

where K is the number of targets that reflect the signals back to the radar receiver, $\{\beta_k\}$ are complex amplitudes proportional to the radar cross sections (RCSs) of those targets, $\{\theta_k\}$ are the target location parameters, $\epsilon(n)$ denotes the interference-plus-noise term, and $(\cdot)^c$ denotes the complex conjugate. The unknown parameters, to be estimated from $\{\mathbf{y}(n)\}_{n=1}^N$, are $\{\beta_k\}_{k=1}^K$ and $\{\theta_k\}_{k=1}^K$.

The problem of interest here is to determine the maximum number of targets that can be uniquely identified, to devise parametric and nonparametric approaches to estimate the target parameters, and to provide flexible transmit beampattern designs by optimizing the covariance of matrix of $\mathbf{x}(n)$ under practical constraints.

1.3 PARAMETER IDENTIFIABILITY

Parameter identifiability is basically a consistency aspect: we want to establish the uniqueness of the solution to the parameter estimation problem as either the signal-to-interference-plus-noise ratio (SINR) or the snapshot number N goes to infinity [18]. It is clear that in either case, assuming that the interference-plus-noise term $\epsilon(n)$ is uncorrelated with $\mathbf{x}(n)$, the identifiability property of the first term in (1.6) is not affected by the second term. In particular, it follows that asymptotically we can handle any number of interferences; of course, for a finite snapshot number N and a finite SINR, the accuracy will degrade as the number of interferences increases, but that is a different issue — the parameter identifiability is *not* affected.

1.3.1 Preliminary Analysis

The "identifiability equation" is as follows:

$$\sum_{k=1}^{K} \breve{\beta}_k \mathbf{b}^c(\breve{\theta}_k)\mathbf{a}^*(\breve{\theta}_k)\mathbf{x}(n) = \sum_{k=1}^{K} \beta_k \mathbf{b}^c(\theta_k)\mathbf{a}^*(\theta_k)\mathbf{x}(n), \quad n = 1, \ldots, N \tag{1.7}$$

For the identifiability of parameters to hold, (1.7) should have a unique solution: $\breve{\beta}_k = \beta_k$, $\breve{\theta}_k = \theta_k$, $k = 1, \ldots, K$. Assume that the M_t transmitted waveforms are linearly independent of each other, which implies that

$$\operatorname{rank}\{[\mathbf{x}(1) \cdots \mathbf{x}(N)]\} = M_t \tag{1.8}$$

Then (1.7) is equivalent to

$$\sum_{k=1}^{K} \breve{\beta}_k \mathbf{b}^c(\breve{\theta}_k)\mathbf{a}^*(\breve{\theta}_k) = \sum_{k=1}^{K} \beta_k \mathbf{b}^c(\theta_k)\mathbf{a}^*(\theta_k) \tag{1.9}$$

or

$$\breve{\mathbf{A}}\breve{\boldsymbol{\beta}} = \mathbf{A}\boldsymbol{\beta} \tag{1.10}$$

where

$$\boldsymbol{\beta} = [\beta_1 \ \cdots \ \beta_K]^T \tag{1.11}$$

$$\breve{\boldsymbol{\beta}} = [\breve{\beta} \ \cdots \ \breve{\beta}_K]^T \tag{1.12}$$

$$\mathbf{A} = [\mathbf{a}^c(\theta_1) \otimes \mathbf{b}^c(\theta_1) \ \cdots \ \mathbf{a}^c(\theta_K) \otimes \mathbf{b}^c(\theta_K)] \tag{1.13}$$

and

$$\breve{\mathbf{A}} = [\mathbf{a}^c(\breve{\theta}_1) \otimes \mathbf{b}^c(\breve{\theta}_1) \ \cdots \ \mathbf{a}^c(\breve{\theta}_K) \otimes \mathbf{b}^c(\breve{\theta}_K)] \tag{1.14}$$

with the symbol $\otimes$ denoting the Krönecker product operator, and $\mathbf{a}^c \otimes \mathbf{b}^c$ denoting the virtual steering vector of the MIMO radar.

In the next subsection we present conditions for the uniqueness of the solution to (1.10). However, before doing so, we discuss some features of (1.10) based on several examples of special cases of MIMO radar. First, consider the case where the transmit array is also the receive array, which in particular implies that $M_t = M_r \triangleq M$. Then (1.10) may contain quite a few redundant equations. In such a case, we have

$$\mathbf{b}(\theta) = \mathbf{a}(\theta) \tag{1.15}$$

and hence the generic column of $\mathbf{A}$ is the $M^2 \times 1$ vector $\mathbf{a}^c(\theta) \otimes \mathbf{a}^c(\theta)$. For a uniform linear array (ULA), the vector $\mathbf{a}^c(\theta) \otimes \mathbf{a}^c(\theta)$ has only $2M - 1$ distinct elements: 1, $e^{-j\omega}, \ldots, e^{-j(2M-1)\omega}$, where $\omega = 2\pi f_0 \tau(\theta)$, where $\tau(\theta)$ is the inter-element delay difference. However, a nonuniform but still linear array may have up to $(M^2 + M)/2$ distinct elements. For example, this is the case for the minimum redundancy linear array [32] with $M = 4$ and $\mathbf{a}^c(\theta) = [1 \quad e^{-j\omega} \quad e^{-j4\omega} \quad e^{-j6\omega}]^T$.

Next, consider the more general case of $M_r \neq M_t$ and of possibly different receive and transmit arrays. When the transmit (receive) array is a ULA that is a contiguous subset of the receive (transmit) ULA, $\mathbf{b}^c(\theta) \otimes \mathbf{a}^c(\theta)$ has only $M_t + M_r - 1$ distinct elements; in fact, this appears to be the smallest possible number of distinct elements. When the transmit and receive arrays share few or no antennas, all equations of (1.10) may well be distinct. For example, let

$$\mathbf{b}^c(\theta) = [1 \quad e^{-j\omega} \quad \cdots \quad e^{-j(M_r-1)\omega}]^T \tag{1.16}$$

and

$$\mathbf{a}^c(\theta) = [1 \quad e^{-jM_r\omega} \quad \cdots \quad e^{-j(M_t-1)M_r\omega}]^T \tag{1.17}$$

Then

$$\mathbf{b}^c(\theta) \otimes \mathbf{a}^c(\theta) = [1 \quad e^{-j\omega} \quad \cdots \quad e^{-j(M_tM_r-1)\omega}]^T \tag{1.18}$$

which is a (virtual) ULA with M_tM_r elements.

1.3.2 Sufficient and Necessary Conditions

Let

$$\breve{\mathbf{B}}\breve{\boldsymbol{\beta}} = \mathbf{B}\boldsymbol{\beta} \tag{1.19}$$

denote the system of equations in (1.10) from which the identical equations have been eliminated. Let $\mathbf{c}(\theta)$ denote a (generic) column of $\mathbf{B}$, and let L_c denote the dimension of $\mathbf{c}(\theta)$. Then, according to the discussion at the end of Section 1.3.1, we obtain

$$L_c \in [M_t + M_r - 1,\ \ M_t M_r] \tag{1.20}$$

Using results from Refs. 33 and 34, we can show that when the M_t transmitted waveforms are linearly indepenent of each other [as assumed before; see (1.8)], a *sufficient and generically* (*for almost every vector* β) *necessary condition for parameter identifiability* is

$$L_c + 1 > 2K, \quad \text{i.e.,} \quad K_{\max} = \left\lceil \frac{L_c - 1}{2} \right\rceil \tag{1.21}$$

where $\lceil \cdot \rceil$ denotes the smallest integer greater than or equal to a given number. In view of (1.20), we thus have

$$K_{\max} \in \left[\frac{M_t + M_r - 2}{2},\ \frac{M_t M_r + 1}{2} \right) \tag{1.22}$$

depending on the array geometry and on how many antennas are shared between the transmit and receive arrays [18].

Furthermore, generically (i.e., for almost any vector β), the identifiability can be ensured under the following condition [18,34]

$$L_c > \frac{3}{2}K, \quad \text{i.e.,} \quad K_{\max} = \left\lceil \frac{2L_c - 3}{3} \right\rceil \tag{1.23}$$

and, similarly to (1.22), we have

$$K_{\max} \in \left[\frac{2(M_t + M_r) - 5}{3},\ \frac{2M_t M_r}{3} \right) \tag{1.24}$$

[which, typically, yields a larger number $K_{\max}$ than the one given in (1.22)].

For a phased-array radar (which uses M_r receiving antennas, and for which we can basically assume that $M_t = 1$), the condition similar to (1.22) is

$$K_{\max} = \left\lceil \frac{M_r - 1}{2} \right\rceil \tag{1.25}$$

and that similar to (1.24) is

$$K_{\max} = \left\lceil \frac{2M_r - 3}{3} \right\rceil \tag{1.26}$$

Hence, the maximum number of targets that can be uniquely identified by a MIMO radar can be up to M_t times that of its phased-array counterpart. To illustrate the extreme cases, note that when a filled [i.e., half-wavelength (0.5λ) inter-element spacing] uniform linear array (ULA) is used for both transmitting and receiving, which appears to be the worst MIMO radar scenario from the parameter identifiability standpoint, the maximum number of targets that can be identified by the MIMO radar is about twice that of its phased-array counterpart. This is because the virtual aperture $\mathbf{b}^c(\theta) \otimes \mathbf{a}^c(\theta)$ of the MIMO radar system has only $M_t + M_r - 1$ distinct elements. On the other hand, when the receive array is a filled ULA with M_r elements and the transmit array is a sparse ULA comprising M_t elements with $M_r/2$-wavelength inter-element spacing, the virtual aperture of the MIMO radar system is a filled (M_tM_r)-element ULA; that is, the virtual aperture length is M_t times that of the receive array [9,18]. This increased virtual aperture size leads to the result that the maximum number of targets that can be uniquely identified by the MIMO radar is M_t times that of its phased-array counterpart.

1.3.3 Numerical Examples

We present several numerical examples to demonstrate the parameter identifiability of MIMO radar, as compared to its phased-array counterpart. First, consider a MIMO radar system where a ULA with $M_t = M_r = M = 10$ antennas and half-wavelength spacing between adjacent antennas is used both for transmitting and for receiving. The transmitted waveforms are orthogonal to each other. Consider a scenario in which K targets are located at $\theta_1 = 0^\circ, \theta_2 = 10^\circ, \theta_3 = -10^\circ, \theta_4 = 20^\circ, \theta_5 = -20^\circ, \theta_6 = 30^\circ, \theta_7 = -30^\circ, \ldots,$ with identical complex amplitudes $\beta_1 = \cdots = \beta_K = 1$. The number of snapshots is $N = 256$. The received signal is corrupted by a spatially and temporally white circularly symmetric complex Gaussian noise with mean zero and variance 0.01 (i.e., $\text{SNR} = 20\,\text{dB}$) and by a jammer located at 45° with an unknown waveform (uncorrelated with the waveforms transmitted by the radar) with a variance equal to 1 (i.e., $\text{INR} = 20\,\text{dB}$).

Consider the Cramér–Rao bound (CRB) of $\{\theta_k\}$, which gives the best performance of an unbiased estimator. By assuming that $\{\boldsymbol{\epsilon}(n)\}_{n=1}^N$ in (6) are independently and identically distributed (i.i.d.) circularly symmetric complex Gaussian random vectors with mean zero and unknown covariance $\mathbf{Q}$, the CRB for $\{\theta_k\}$ can be obtained using the Slepian–Bangs formula [31]. Figure 1.2a shows the CRB of θ_1 for the MIMO radar as a function of K. For comparison purposes, we also provide the CRB of its phased-array counterpart, for which all the parameters are the same as for the MIMO radar except that $M_t = 1$ and that the amplitude of the transmitted waveform is adjusted so that the total transmission power does not change. Note that the phased-array CRB

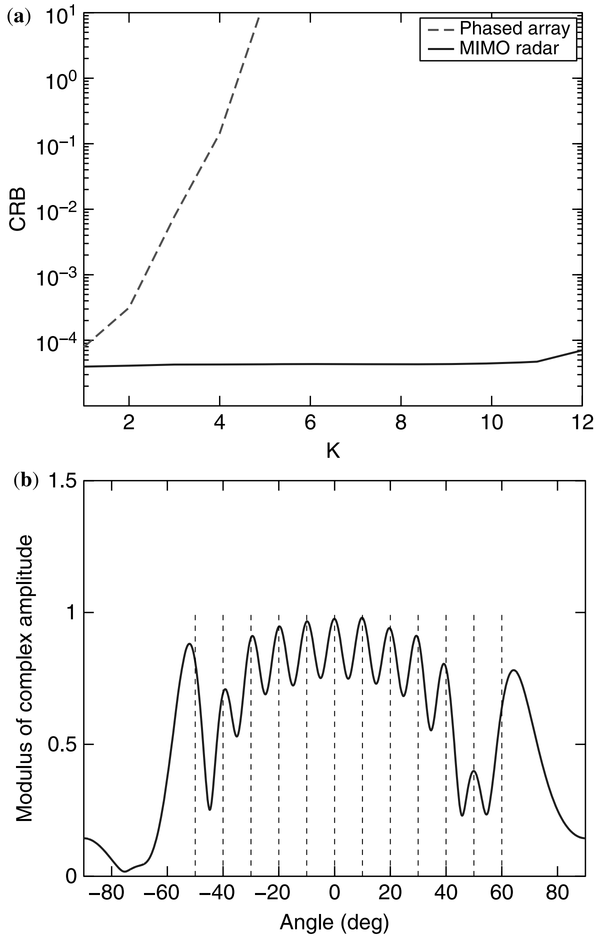

Figure 1.2 Performance of a MIMO radar system where a ULA with $M = 10$ antennas and 0.5-wavelength interelement spacing is used for both transmitting and receiving: (a) Cramér–Rao bound of θ_1 versus K; (b) LS spatial spectrum when $K = 12$.

increases rapidly as K increases from 1 to 6. The corresponding MIMO CRB, however, is almost constant when K is varied from 1 to 12 (but becomes unbounded for $K > 12$). Both results are consistent with the parameter identifiability analysis: $K_{\max} \leq 6$ for the phased-array radar and $K_{\max} \leq 12$ for the MIMO radar.

We next consider a simple nonparametric data-independent least-squares (LS) method [28] [see also Eq. (1.30)] for MIMO radar parameter estimation. Figure 1.2b shows the LS spatial spectrum as a function θ, when $K = 12$. Note that all 12 target locations can be approximately determined from the peak locations of the LS spatial spectrum.

Consider now a MIMO radar system with $M_t = M_r = 5$ antennas. The distance between adjacent antennas is 0.5λ for the receiving ULA and 2.5λ for the transmitting ULA. We retain all the simulation parameters corresponding to Fig. 1.2 except that the targets are located at $\theta_1 = 0^\circ$, $\theta_2 = 8^\circ$, $\theta_3 = -8^\circ$, $\theta_4 = 16^\circ$, $\theta_5 = -16^\circ$, $\theta_6 = 24^\circ$, $\theta_7 = -24^\circ, \ldots$ in this example. Figure 1.3a shows the CRB of θ_1, for both the MIMO radar and the phased-array counterpart, as a function of K. Again, the MIMO CRB is much lower than the phased-array CRB. The behavior of both CRBs is consistent with the parameter identifiability analysis: $K_{\max} \leq 3$ for the phased-array radar and $K_{\max} \leq 16$ for the MIMO radar. Moreover, the

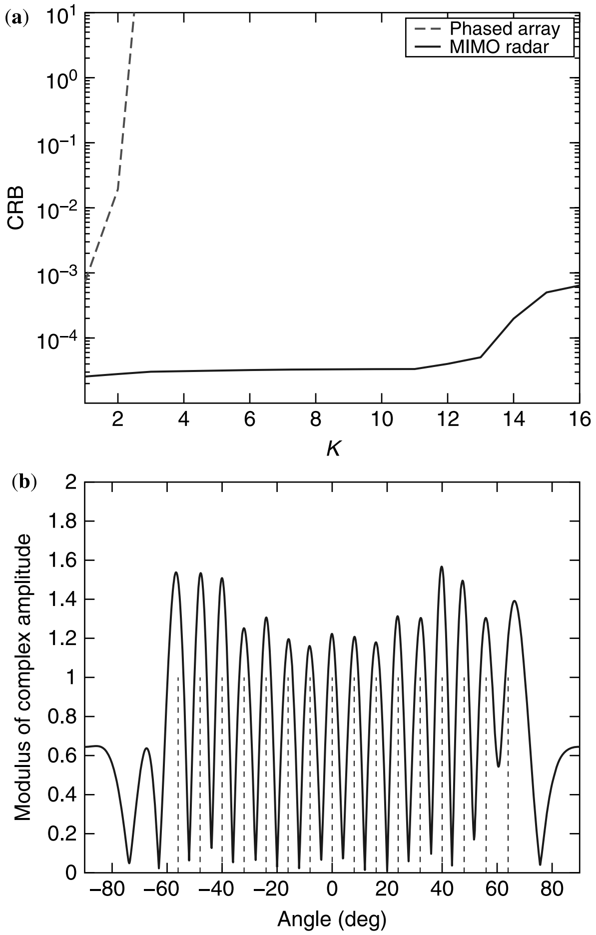

Figure 1.3 Performance of a MIMO radar system with $M_t = M_r = 5$ antennas, and with half-wavelength interelement spacing for the receive ULA and 2.5-wavelength interelement spacing for the transmit ULA: (a) Cramér–Rao bound of θ_1 versus K; (b) LS spatial spectrum when $K = 16$.

parameters of all $K = 16$ targets can be approximately determined with the simple LS method, as shown in Fig. 1.3b.

1.4 NONPARAMETRIC ADAPTIVE TECHNIQUES FOR PARAMETER ESTIMATION

As shown in Refs. 26–28, a MIMO radar makes it possible to use *adaptive* localization and detection techniques directly, unlike a phased-array radar. This is another significant advantage of a MIMO radar system since adaptive techniques are known to have much better resolution and much better interference rejection capability than their data-independent counterparts. For example, in spacetime adaptive processing applications, secondary range bins are needed to be able to use adaptive techniques [35–37]; however, selecting quality secondary range bins is in itself a major challenge [38]. Since the MIMO-probing signals reflected back by the targets are actually linearly independent of each other, the direct application of adaptive techniques is made possible for a MIMO radar system without the need for secondary range bins or even for range compression [19,29].

Let

$$\tilde{\mathbf{A}} = [\beta_1^* \mathbf{a}(\theta_1) \quad \beta_2^* \mathbf{a}(\theta_2) \quad \cdots \quad \beta_K^* \mathbf{a}(\theta_K)] \tag{1.27}$$

Then the sample covariance matrix of the target reflected waveforms is $\tilde{\mathbf{A}}^* \hat{\mathbf{R}}_{xx} \tilde{\mathbf{A}}$, where

$$\hat{\mathbf{R}}_{xx} = \frac{1}{N} \sum_{n=1}^{N} \mathbf{x}(n)\mathbf{x}^*(n) \tag{1.28}$$

is the sample covariance matrix of the transmitted waveforms. When orthogonal waveforms are used for MIMO probing, for example, and $N \geq M_t$, then $\hat{\mathbf{R}}_{xx}$ is a scaled identity matrix. Then $\tilde{\mathbf{A}}^* \tilde{\mathbf{R}}_{xx} \tilde{\mathbf{A}}$ has full rank; in other words, the target reflected waveforms are not completely correlated with each other (or coherent), if the columns of $\tilde{\mathbf{A}}$ are linearly independent of each other, which requires that $K \leq M_t$. The fact that the target reflected waveforms are noncoherent allows the direct application of many adaptive techniques for target localization [28].

Let θ be the location parameter of a generic target, for example, the direction of arrival (DOA) when the targets are in the far field of the arrays. We express the signal matrix at the output of the receiving array in the form

$$\mathbf{Y} = \mathbf{b}^c(\theta)\beta(\theta)\mathbf{a}^*(\theta)\mathbf{X} + \mathbf{Z} \tag{1.29}$$

where $\mathbf{X} = [\,\mathbf{x}(1) \quad \mathbf{x}(2) \quad \cdots \quad \mathbf{x}(N)]$, the columns of $\mathbf{Y} \in \mathcal{C}^{M_r \times N}$ are the received data samples $\{\mathbf{y}(n)\}_{n=1}^{N}$, and $\beta(\theta) \in \mathcal{C}$ denotes the complex amplitude of the reflected signal from θ, which is proportional to the radar cross section (RCS) of the focal point θ.

The matrix $\mathbf{Z} \in \mathcal{C}^{M_r \times N}$ denotes the residual term, which includes the unmodeled noise, interferences from targets at locations other than θ and at other range bins, and intentional or unintentional jamming. For notational simplicity, we do not explicitly show the dependence of $\mathbf{Z}$ on θ.

The problem is to estimate $\beta(\theta)$ for each θ of interest from the observed data matrix $\mathbf{Y}$. The estimates of $\{\beta(\theta)\}$ can be used to form a spatial spectrum. We can then estimate the locations of the targets and their complex amplitudes by searching for the peaks in the so-obtained spectrum.

Note that in (1.29) we consider a particular range bin of interest, whose time of arrival (TOA) is known a priori. This data model can be readily extended to the unknown TOA case by including an unknown TOA parameter τ in $\mathbf{X}$. By estimating β for each θ and τ using the presented methods, we can form a two-dimensional (2D) radar image, whose peaks will indicate existence of targets and their locations (DOA and TOA). Note also that, compared with the conventional techniques, where pulse compression is done separately, the range compression step is implicit in the following proposed methods.

1.4.1 Absence of Array Calibration Errors

A simple way to estimate $\beta(\theta)$ in (1.29) is via the least-squares (LS) method

$$\hat{\beta}_{\mathrm{LS}}(\theta) = \frac{\mathbf{b}^T(\theta)\mathbf{Y}\mathbf{X}^*\,\mathbf{a}(\theta)}{N\,||\mathbf{b}(\theta)||^2[\mathbf{a}^*(\theta)\hat{\mathbf{R}}_{xx}\mathbf{a}(\theta)]} \tag{1.30}$$

where $||\cdot||$ denotes the Euclidean norm. However, as any other data-independent beamforming-type method, the LS method suffers from high sidelobes and low resolution. In the presence of strong interference and jamming, this method completely fails to work.

We present below several data-dependent beamforming-based methods, which, as shown via numerical examples in Section 1.4.3, have much higher resolution and much better interference rejection capability than does the LS method.

1.4.1.1 Capon The Capon estimator consists of two main steps: (1) the Capon beamforming step [31,39] and (2) a LS estimation step, which involves basically a matched filtering.

The Capon beamformer can be formulated as follows

$$\min_{\mathbf{w}} \mathbf{w}^*\hat{\mathbf{R}}_{yy}\mathbf{w} \quad \text{subject to} \quad \mathbf{w}^*\mathbf{b}^c(\theta) = 1 \tag{1.31}$$

where $\mathbf{w} \in C^{M_r \times 1}$ is the weight vector used to achieve noise, interference, and jamming suppression while keeping the desired signal undistorted; and $\hat{\mathbf{R}}_{yy}$ is the sample covariance matrix of the observed data samples:

$$\hat{\mathbf{R}}_{yy} = \frac{1}{N}\mathbf{Y}\mathbf{Y}^* \tag{1.32}$$

Following Refs. 31 and 39, we can readily obtain the solution to (1.31) as follows:

$$\hat{\mathbf{w}}_{\text{Capon}} = \frac{\hat{\mathbf{R}}_{yy}^{-1}\mathbf{b}^c(\theta)}{\mathbf{b}^T(\theta)\hat{\mathbf{R}}_{yy}^{-1}\mathbf{b}^c(\theta)} \tag{1.33}$$

The output of the Capon beamformer is thus given by

$$\frac{\mathbf{b}^T(\theta)\hat{\mathbf{R}}_{yy}^{-1}\mathbf{Y}}{\mathbf{b}^T(\theta)\hat{\mathbf{R}}_{yy}^{-1}\mathbf{b}^c(\theta)} \tag{1.34}$$

Substituting (1.29) into (1.34) yields

$$\frac{\mathbf{b}^T(\theta)\hat{\mathbf{R}}_{yy}^{-1}\mathbf{Y}}{\mathbf{b}^T(\theta)\hat{\mathbf{R}}_{yy}^{-1}\mathbf{b}^c(\theta)} = \beta(\theta)\mathbf{a}^*(\theta)\mathbf{X} + \frac{\mathbf{b}^T(\theta)\hat{\mathbf{R}}_{yy}^{-1}\mathbf{Z}}{\mathbf{b}^T(\theta)\hat{\mathbf{R}}_{yy}^{-1}\mathbf{b}^c(\theta)} \tag{1.35}$$

Applying the LS method to (1.35), we get the Capon estimate of $\beta(\theta)$ as follows:

$$\hat{\beta}_{\text{Capon}}(\theta) = \frac{\mathbf{b}^T(\theta)\,\hat{\mathbf{R}}_{yy}^{-1}\mathbf{Y}\mathbf{X}^*\,\mathbf{a}(\theta)}{N\,[\mathbf{b}^T(\theta)\hat{\mathbf{R}}_{yy}^{-1}\mathbf{b}^c(\theta)][\mathbf{a}^*(\theta)\hat{\mathbf{R}}_{xx}\mathbf{a}(\theta)]} \tag{1.36}$$

where $\hat{\mathbf{R}}_{xx}$ is defined in (1.28). Note that (1.36) is a function of θ. In practice, we need to compute (1.36) for each θ of interest to form a spatial spectrum.

1.4.1.2 APES The amplitude and phase estimation (APES) approach [40–42] is a nonparametric spectral analysis method with superior estimation accuracy [43,44]. We apply this method to the proposed MIMO radar system to achieve better amplitude estimation accuracy.

By following Ref. 41, we can formulate the APES method as

$$\min_{\mathbf{w},\beta} \|\, \mathbf{w}^*\mathbf{Y} - \beta(\theta)\mathbf{a}^*(\theta)\mathbf{X}\,\|^2 \quad \text{subject to} \quad \mathbf{w}^*\mathbf{b}^c(\theta) = 1 \tag{1.37}$$

where $\mathbf{w} \in C^{M_r\times 1}$ is the weight vector. Intuitively, the goal of (1.37) is to find a beamformer whose output is as close as possible to a signal with the waveform given by $\mathbf{a}^*(\theta)\,\mathbf{X}$.

Minimizing the cost function in (1.37) with respect to $\beta(\theta)$ yields

$$\hat{\beta}_{\text{APES}}(\theta) = \frac{\mathbf{w}^*\mathbf{Y}\mathbf{X}^*\mathbf{a}(\theta)}{N\,\mathbf{a}^*(\theta)\hat{\mathbf{R}}_{xx}\mathbf{a}(\theta)} \tag{1.38}$$

Then the optimization problem in (1.37) reduces to

$$\min_{\mathbf{w}} \mathbf{w}^* \hat{\mathbf{Q}} \mathbf{w} \quad \text{subject to} \quad \mathbf{w}^* \mathbf{b}^c(\theta) = 1 \tag{1.39}$$

with

$$\hat{\mathbf{Q}} = \hat{\mathbf{R}}_{yy} - \frac{\mathbf{Y}\mathbf{X}^* \, \mathbf{a}(\theta)\mathbf{a}^*(\theta)\mathbf{X}\mathbf{Y}^*}{N^2 \, \mathbf{a}^*(\theta)\hat{\mathbf{R}}_{xx}\mathbf{a}(\theta)} \tag{1.40}$$

Solving the optimization problem in (1.39) gives the APES beamformer weight vector [41]:

$$\hat{\mathbf{w}}_{\mathrm{APES}} = \frac{\hat{\mathbf{Q}}^{-1}\mathbf{b}^c(\theta)}{\mathbf{b}^T(\theta)\hat{\mathbf{Q}}^{-1}\mathbf{b}^c(\theta)} \tag{1.41}$$

By inserting (1.41) into (1.38), the APES estimate of $\beta(\theta)$ is readily obtained as

$$\hat{\beta}_{\mathrm{APES}}(\theta) = \frac{\mathbf{b}^T(\theta)\hat{\mathbf{Q}}^{-1}\mathbf{Y}\mathbf{X}^* \, \mathbf{a}(\theta)}{N \, [\mathbf{b}^T(\theta)\hat{\mathbf{Q}}^{-1}\mathbf{b}^c(\theta)] \, [\mathbf{a}^*(\theta)\hat{\mathbf{R}}_{xx}\mathbf{a}(\theta)]} \tag{1.42}$$

Note that the only difference between the Capon estimator and the APES estimator is that the sample covariance matrix $\hat{\mathbf{R}}_{yy}$ in (1.36) is replaced in (1.42) by the residual covariance estimate $\hat{\mathbf{Q}}$. However, this seemingly minor difference makes these two methods behave quite differently (see, e.g., Section 1.4.3).

1.4.1.3 CAPES and CAML As discussed in Ref. 40 (see also Section 1.4.3), the two data-dependent methods described above behave differently. Capon has high resolution, and hence can provide accurate estimates of the target locations. However, the Capon amplitude estimates are significantly biased downward. The APES estimator gives much more accurate amplitude estimates at the target locations, but at the cost of lower resolution (i.e., greater minimum distance needed for two targets to be resolved). To reap the benefits of both Capon and APES, an alternative estimation procedure, referred to as *CAPES*, has been proposed [45]. CAPES first estimates the peak locations using the Capon estimator and then refines the amplitude estimates at these locations using the APES estimator. CAPES can be directly applied to the MIMO radar target localization and amplitude estimation problem considered here.

Inspired by the CAPES method, we propose below a new approach, referred to as CAML, which combines Capon and the more recently proposed approximate maximum likelihood (AML) estimator based on a diagonal growth curve (DGC) model [46]. In CAML, AML, instead of APES, is used to estimate the target amplitudes at the target locations estimated by Capon. Since, unlike APES, AML estimates the amplitudes of all targets at the given locations jointly rather than one at a time, the latter can provide better estimation accuracy than can the former.

Let $\hat{\theta}_k(k = 1, 2, \ldots, K)$ denote the estimated target locations, that is, the peak locations of the spatial spectrum estimated by Capon. Here K is assumed known. If K is unknown, it can be determined accurately using a generalized likelihood ratio test (GLRT), the details of which are given in the Appendix 1A. Let

$$\mathbf{A}_r = [\mathbf{b}(\hat{\theta}_1)\,\mathbf{b}(\hat{\theta}_2)\ \cdots\ \mathbf{b}(\hat{\theta}_K)] \tag{1.43}$$

$$\mathbf{A}_t = [\mathbf{a}(\hat{\theta}_1)\ \mathbf{a}(\hat{\theta}_2)\ \cdots\ \mathbf{a}(\hat{\theta}_K)] \tag{1.44}$$

and

$$\beta = [\beta(\hat{\theta}_1)\ \beta(\hat{\theta}_2)\ \cdots\ \beta(\hat{\theta}_K)]^T \tag{1.45}$$

Then the data model in (1.29) can be reformulated as a DGC model [46]:

$$\mathbf{Y} = \mathbf{A}_r^c \mathbf{B}(\mathbf{A}_t^* \mathbf{X}) + \tilde{\mathbf{Z}} \quad \text{with} \quad \mathbf{B} = \operatorname{diag}(\beta) \tag{1.46}$$

In (1.46), diag(β) denotes a diagonal matrix whose diagonal elements are equal to the elements of β, and $\tilde{\mathbf{Z}}$ is the residual term, whose columns are assumed to be independently and identically distributed (i.i.d.) circularly symmetric complex Gaussian random vectors with mean zero and unknown covariance matrix. Since the maximum-likelihood (ML) estimate of β in (1.46) cannot be produced in closed form, we use the AML estimator [46] instead, which is asymptotically equivalent to the ML for a large data sample number N.

By using the AML method in Eq. (18) of Ref. 46, the estimate of β can be readily obtained as

$$\hat{\beta}_{\text{AML}} = \frac{1}{N}\left[(\mathbf{A}_r^T \mathbf{T}^{-1} \mathbf{A}_r^c) \odot (\mathbf{A}_t^T \hat{\mathbf{R}}_{xx}^c \mathbf{A}_t^c)\right]^{-1} \operatorname{vecd}\left(\mathbf{A}_r^T \mathbf{T}^{-1} \mathbf{Y} \mathbf{X}^* \mathbf{A}_t\right) \tag{1.47}$$

where $\odot$ denotes the Hadamard product [47], vecd($\cdot$) denotes a column vector formed by the diagonal elements of a matrix, and

$$\mathbf{T} = N\,\hat{\mathbf{R}}_{yy} - \frac{1}{N}\mathbf{Y}\mathbf{X}^*\mathbf{A}_t(\mathbf{A}_t^*\hat{\mathbf{R}}_{xx}\mathbf{A}_t)^{-1}\mathbf{A}_t^*\mathbf{X}\mathbf{Y}^* \tag{1.48}$$

1.4.2 Presence of Array Calibration Errors

The previous data-dependent methods assume that the transmitting and receiving arrays are perfectly calibrated, that is, that $\mathbf{a}(\theta)$ and $\mathbf{b}(\theta)$ are accurately known as functions of θ. However, in practice, array calibration errors are often inevitable. The presence of array calibration errors and the related small data sample number problem [48] can significantly degrade the performance of the data-dependent beamforming methods discussed so far.

1.4.2.1 RCB We consider the application of the robust Capon beamformer (RCB) (see Refs. 49–51 and references cited therein) to a MIMO radar system that suffers from calibration errors. RCB allows $\mathbf{b}(\theta)$ to lie in an uncertainty set. Without loss of generality, we assume that $\mathbf{b}(\theta)$ belongs to an uncertainty sphere

$$\| \mathbf{b}(\theta) - \bar{\mathbf{b}}(\theta) \|^2 \leq \epsilon_r \tag{1.49}$$

where both $\bar{\mathbf{b}}(\theta)$, the nominal receiving array steering vector, and ϵ_r are given. (For the more general case of ellipsoidal uncertainty sets, see Refs. 49–51 and references cited therein.) Note that the calibration errors in $\mathbf{a}(\theta)$ will also degrade the accuracy of the estimate of $\beta(\theta)$ [see (1.36)]. However, the LS (or matched filtering) approach of (1.36) is quite robust against calibration errors in $\mathbf{a}(\theta)$.

The RCB method is based on the following covariance fitting formulation [49,50,52]

$$\begin{aligned} \max_{\sigma^2(\theta),\mathbf{b}(\theta)} \sigma^2(\theta) \quad \text{subject to} \quad & \hat{\mathbf{R}}_{yy} - \sigma^2(\theta)\mathbf{b}^c(\theta)\mathbf{b}^T(\theta) \geq 0 \\ & \| \mathbf{b}(\theta) - \bar{\mathbf{b}}(\theta) \|^2 \leq \epsilon_r \end{aligned} \tag{1.50}$$

where $\sigma^2(\theta)$ denotes the power of the signal of interest and $\mathbf{P} \geq 0$ means that the matrix $\mathbf{P}$ is positive semidefinite. The optimization problem in (1.50) can be simplified as follows [49]:

$$\min_{\mathbf{b}(\theta)} \mathbf{b}^T(\theta)\hat{\mathbf{R}}_{yy}^{-1}\mathbf{b}^c(\theta) \quad \text{subject to} \quad \| \mathbf{b}(\theta) - \bar{\mathbf{b}}(\theta) \|^2 \leq \epsilon_r \tag{1.51}$$

By using the Lagrange multiplier methodology [49], the solution to (1.51) is found to be

$$\hat{\mathbf{b}}(\theta) = \bar{\mathbf{b}}(\theta) - [\mathbf{I} + \lambda(\theta)\hat{\mathbf{R}}_{yy}^c]^{-1}\bar{\mathbf{b}}(\theta) \tag{1.52}$$

where $\mathbf{I}$ denotes the identity matrix. The Lagrange multiplier $\lambda(\theta) \geq 0$ in (1.52) is obtained as the solution to the constraint equation

$$\| [\mathbf{I} + \lambda(\theta)\hat{\mathbf{R}}_{yy}^c]^{-1} \bar{\mathbf{b}}(\theta) \|^2 = \epsilon_r \tag{1.53}$$

which can be solved efficiently by using the Newton method since the left side of (1.53) is a monotonically decreasing function of $\lambda(\theta)$ (see Ref. 49 for more details). Once the Lagrange multiplier $\lambda(\theta)$ has been determined, $\hat{\mathbf{b}}(\theta)$ can be obtained from (1.52). To eliminate a scaling ambiguity [49], we scale $\hat{\mathbf{b}}(\theta)$ such that $\| \hat{\mathbf{b}}(\theta) \|^2 = M_r$. Replacing $\mathbf{b}(\theta)$ in (1.36) by the scaled steering vector $\hat{\mathbf{b}}(\theta)$ yields the RCB estimate of $\beta(\theta)$.

1.4.2.2 DCRCB A doubly constrained robust Capon beamformer (DCRCB) has been proposed [53]. In the DCRCB, in addition to the spherical constraint in (1.49), the steering vector $\mathbf{b}(\theta)$ is constrained to have a constant norm:

$$\| \mathbf{b}(\theta) \|^2 = M_r \tag{1.54}$$

Then the covariance fitting formulation [see (1.50)] becomes

$$\begin{aligned} \max_{\sigma^2(\theta),\mathbf{b}(\theta)} \sigma^2(\theta) \quad \text{subject to} \quad & \hat{\mathbf{R}}_{yy} - \sigma^2(\theta)\mathbf{b}^c(\theta)\mathbf{b}^T(\theta) \geq 0 \\ & \| \mathbf{b}(\theta) - \bar{\mathbf{b}}(\theta) \|^2 \leq \epsilon_r \\ & \| \mathbf{b}(\theta) \|^2 = M_r \end{aligned} \tag{1.55}$$

The optimization problem in (1.55) can be simplified to [53]

$$\begin{aligned} \min_{\mathbf{b}(\theta)} \mathbf{b}^T(\theta)\hat{\mathbf{R}}_{yy}^{-1}\mathbf{b}^c(\theta) \quad \text{subject to} \quad & \mathrm{Re}[\bar{\mathbf{b}}^T(\theta)\mathbf{b}^c(\theta)] \geq M_r - \frac{\epsilon_r}{2} \\ & \| \mathbf{b}(\theta) \|^2 = M_r \end{aligned} \tag{1.56}$$

where $\mathrm{Re}(\cdot)$ denotes the real part of a complex number. Let $\mathbf{u}_1$ be the principal eigenvector of $\hat{\mathbf{R}}_{yy}$, and let

$$\tilde{\mathbf{b}}^c(\theta) = M_r^{1/2}\,\mathbf{u}_1 \,\exp\{j \arg[\,\mathbf{u}_1^*\bar{\mathbf{b}}^c(\theta)]\} \tag{1.57}$$

with $\arg(\cdot)$ denoting the phase of a complex number. If $\tilde{\mathbf{b}}(\theta)$ in (1.57) satisfies

$$\mathrm{Re}[\bar{\mathbf{b}}^T(\theta)\tilde{\mathbf{b}}^c(\theta)] \geq M_r - \frac{\epsilon_r}{2} \tag{1.58}$$

then, obviously, $\hat{\hat{\mathbf{b}}}(\theta) = \tilde{\mathbf{b}}(\theta)$ is the optimal solution of (1.56). Otherwise, by using the Lagrange multiplier methodology [53], the optimal solution to (1.56) is

$$\hat{\hat{\mathbf{b}}}(\theta) = \left(M_r - \frac{\epsilon_r}{2}\right) \frac{[\hat{\mathbf{R}}_{yy}^{-c} + \lambda(\theta)\mathbf{I}]^{-1}\,\bar{\mathbf{b}}(\theta)}{\bar{\mathbf{b}}^*(\theta)\,[\hat{\mathbf{R}}_{yy}^{-c} + \lambda(\theta)\mathbf{I}]^{-1}\,\bar{\mathbf{b}}(\theta)} \tag{1.59}$$

where $(\cdot)^{-c} = [(\cdot)^c]^{-1}$. The Lagrange multiplier $\lambda(\theta)$ in (1.59), which can be negative, is obtained as the solution to the constraint equation

$$\frac{\bar{\mathbf{b}}^T(\theta)\,[\hat{\mathbf{R}}_{yy}^{-1} + \lambda(\theta)\mathbf{I}]^{-2}\,\bar{\mathbf{b}}^c(\theta)}{\left\{\bar{\mathbf{b}}^T(\theta)\,[\hat{\mathbf{R}}_{yy}^{-1} + \lambda(\theta)\mathbf{I}]^{-1}\,\bar{\mathbf{b}}^c(\theta)\right\}^2} = -\frac{M_r}{(M_r - (\epsilon_r/2))^2} \tag{1.60}$$

As in the case of RCB, the constraint equation (1.60) can be solved efficiently by using the Newton method since the left side of (1.60) is a monotonically decreasing function of $\lambda(\theta)$ (see Ref. 53 for more details).

We summarize the DCRCB estimator of $\beta(\theta)$ as follows:

1. Compute $\tilde{\mathbf{b}}(\theta)$ by (1.57).
2. Assuming that $\tilde{\mathbf{b}}(\theta)$ satisfies (1.58), estimate $\beta(\theta)$ by replacing $\mathbf{b}(\theta)$ in (1.36) by $\hat{\hat{\mathbf{b}}}(\theta) = \tilde{\mathbf{b}}(\theta)$, and stop.
3. Assuming that (1.58) is not satisfied, solve (1.60) for $\lambda(\theta)$. Calculate $\hat{\hat{\mathbf{b}}}(\theta)$ by (1.59) using the so-obtained $\lambda(\theta)$.
4. Compute the DCRCB estimate of $\beta(\theta)$ by replacing $\mathbf{b}(\theta)$ in (1.36) by $\hat{\hat{\mathbf{b}}}(\theta)$, and stop.

1.4.3 Numerical Examples

Consider a MIMO radar system where a uniform linear array with $M_t = M_r = M = 10$ antennas and half-wavelength spacing between adjacent antennas is used for both transmitting and receiving. The transmitted waveforms (rows of $\mathbf{X}$) are orthogonal quadrature phase-shift-keyed (QPSK) sequences, and hence we have $\hat{\mathbf{R}}_{xx} = \mathbf{I}$ (this choice of $\hat{\mathbf{R}}_{xx}$ is optimal in a maximum-SNR sense [54]). Consider a scenario in which $K = 3$ targets are located at $\theta_1 = -40^\circ$, $\theta_2 = -25^\circ$, and $\theta_3 = -10^\circ$ with complex amplitudes $\beta_1 = 4$, $\beta_2 = 4$, and $\beta_3 = 1$, respectively. There is a strong jammer at 0° with an unknown waveform and with amplitude 1000 (i.e., 60 dB above β_3). The received signal has $N = 256$ data samples and is corrupted by a zero-mean spatially colored Gaussian noise with an unknown covariance matrix. The (p,q)th element of the unknown noise covariance matrix is $(1/\mathrm{SNR})0.9^{|p-q|}e^{j(p-q)\pi/2}$.

We first consider the case of no array calibration errors. Let SNR = 10 dB. The moduli of the spatial spectral estimates of $\beta(\theta)$, versus θ, obtained by using LS, Capon, APES, CAPES, and CAML are given in Figs. 1.4a,b,c,e,f, respectively. For comparison purpose, we also show the true spatial spectrum via dashed lines in these figures. As seen in Fig. 1.4a, the LS method suffers from high sidelobes and low resolution. In the presence of the strong jamming signal, the LS estimator fails to work properly. Capon and APES possess great interference and jamming suppression capabilities. The Capon method gives very narrow peaks around the target locations. However, the Capon amplitude estimates are biased downward. The APES method gives more accurate amplitude estimates around the target locations, but its resolution is slightly worse than that of Capon. Note that in Figs. 1.4a–c a false peak occurs at $\theta = 0^\circ$ owing to the presence of the strong jammer. Although the jammer waveform is statistically independent of the waveforms transmitted by the MIMO radar, a false peak still exists since the jammer is 60 dB stronger than the weakest target and the data sample number is finite.

To reject the false peak, we use a generalized likelihood ratio test (GLRT) for each angle of interest; the generalized likelihood ratio (GLR) is given by (see Appendix 1A for details)

$$\rho(\theta) = 1 - \frac{\mathbf{b}^T(\theta)\hat{\mathbf{R}}_{yy}^{-1}\mathbf{b}^c(\theta)}{\mathbf{b}^T(\theta)\hat{\mathrm{Q}}^{-1}\mathbf{b}^c(\theta)} \tag{1.61}$$

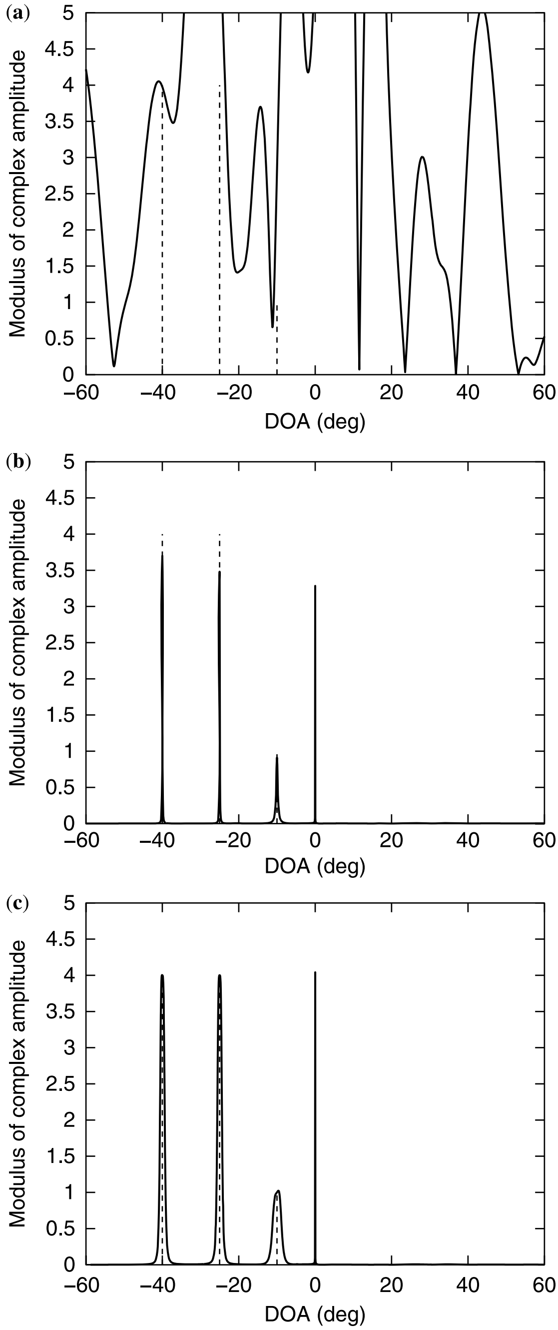

Figure 1.4 Spatial spectral estimates and GLR in the absence of array calibration errors, when $\theta_1 = -40^\circ$, $\theta_2 = -25^\circ$, and $\theta_3 = -10^\circ$: (a) LS; (b) Capon; (c) APES; (d) GLR; (e) CAPES; (f) CAML.

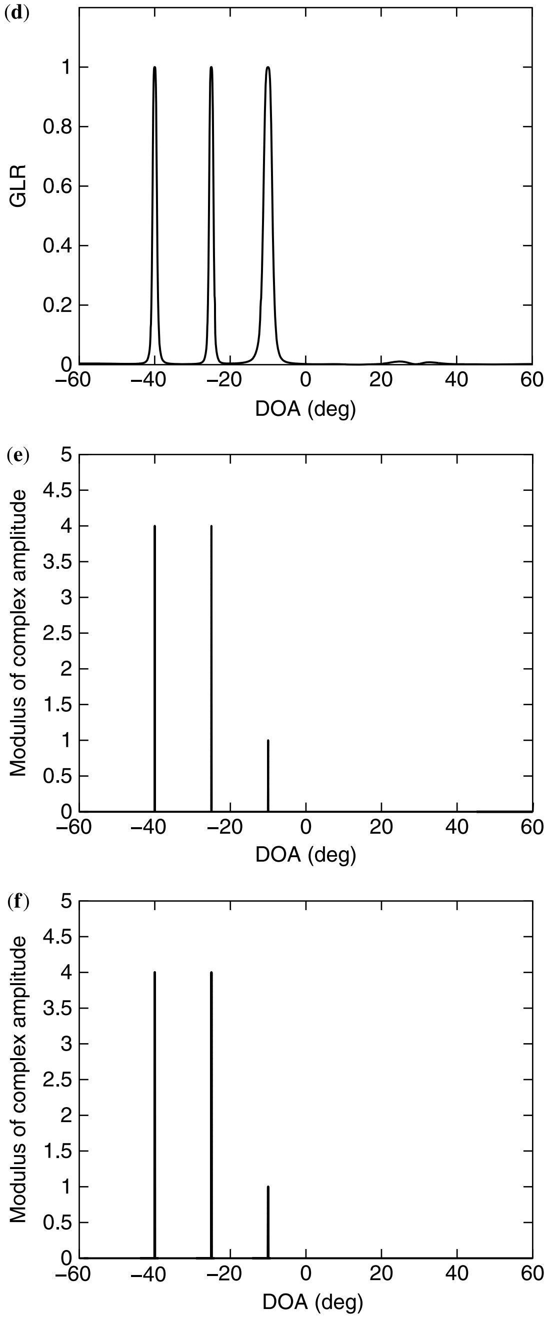

Figure 1.4 *Continued.*

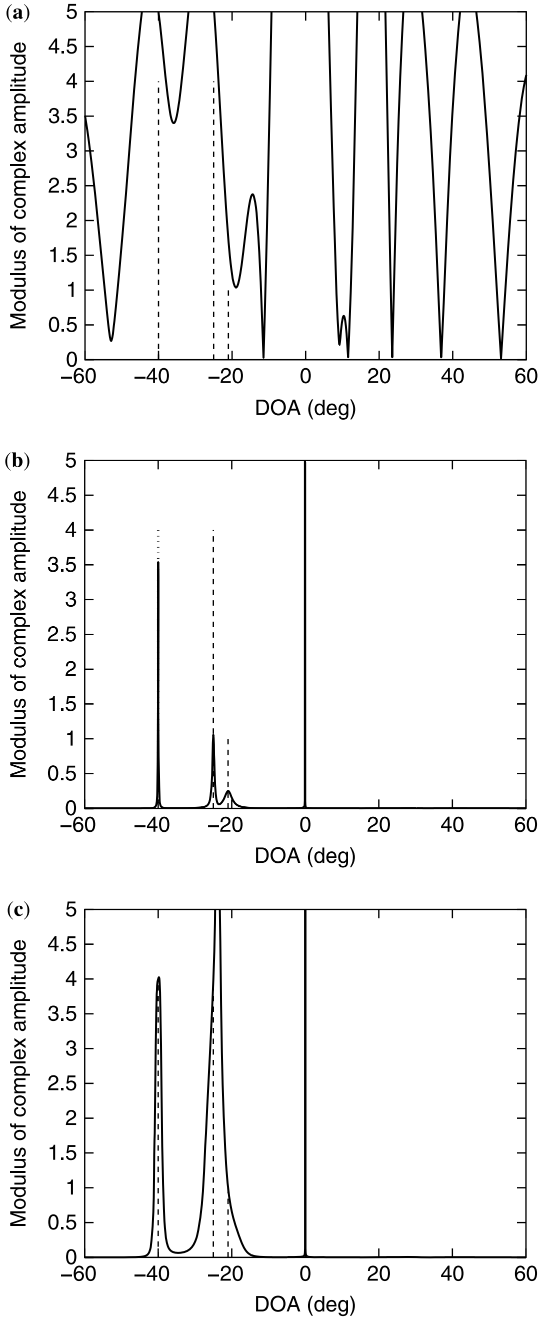

Figure 1.5 Spatial spectral estimates and GLR in the absence of array calibration errors, when $\theta_1 = -40^\circ$, $\theta_2 = -25^\circ$, and $\theta_3 = -21^\circ$: (a) LS; (b) Capon; (c) APES; (d) GLR; (e) CAPES; (f) CAML.

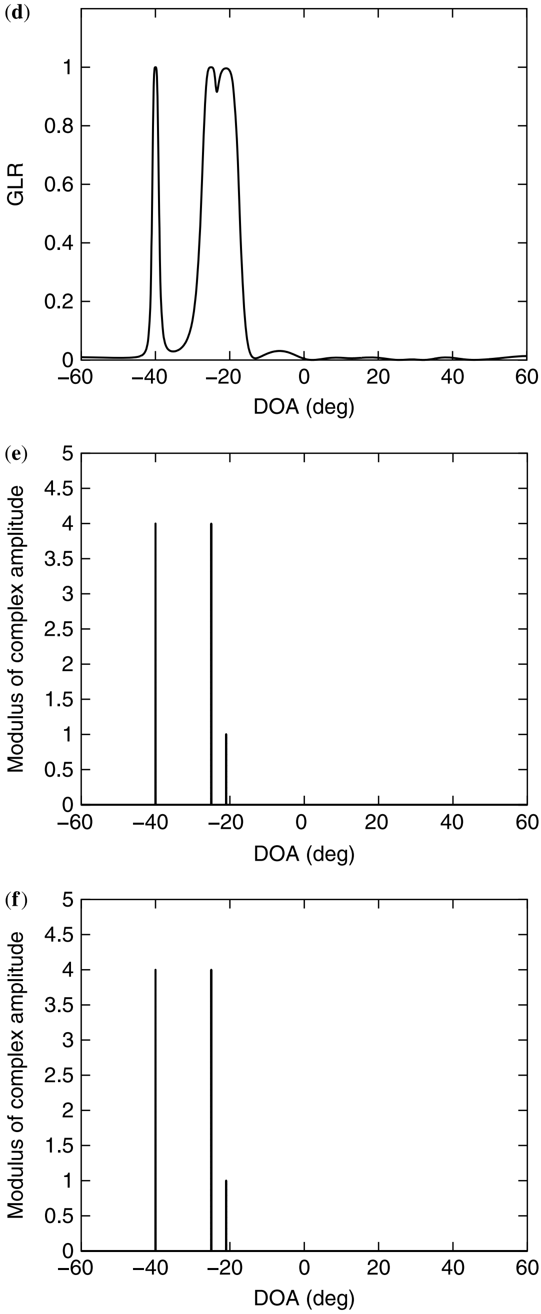

Figure 1.5 *Continued*.

where $\hat{\mathbf{R}}_{yy}$ and $\hat{\mathbf{Q}}$ are as given in (1.32) and (1.40), respectively. Figure 1.4d gives the GLR as a function of the target location parameter θ. As expected, we get high GLRs at the target locations and low GLRs at other locations, including the jammer location. By comparing the GLR with a threshold, the false peak due to the strong jammer can be readily detected and rejected, and a correct estimate of the number of the targets can be obtained. This information can be passed to CAPES and CAML to obtain Figs. 1.4e,f. As seen from these figures, both CAPES and CAML give accurate estimates of the target locations and amplitudes.

Next we consider a more challenging example where θ_3 is -21° while all the other simulation parameters are the same as before. As shown in Fig. 1.5c, in this example

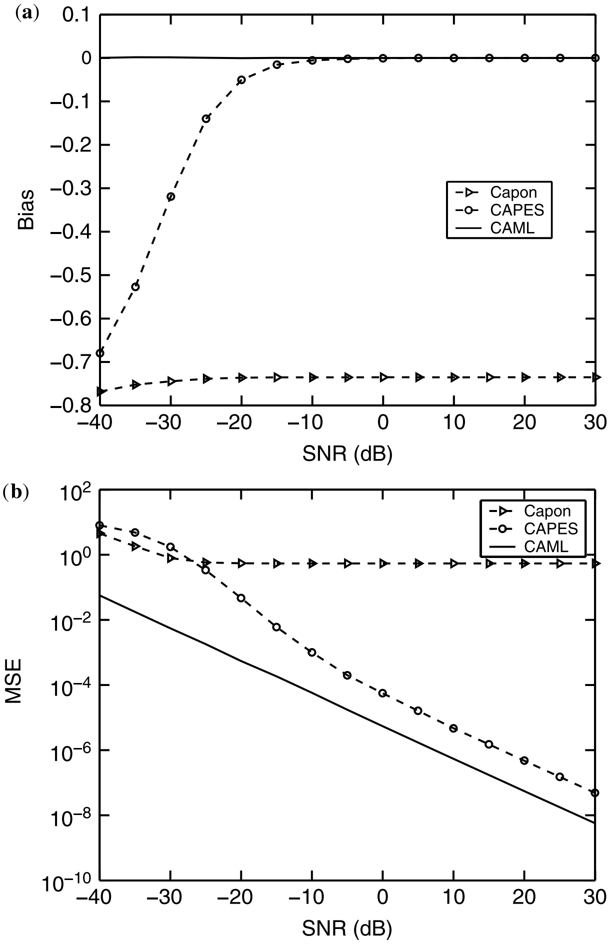

Figure 1.6 Empirical bias and MSE of the amplitude estimate for the target at θ_3 versus SNR, in the absence of array calibration errors, when $\theta_1 = -40^\circ$, $\theta_2 = -25^\circ$, and $\theta_3 = -21^\circ$: (a) bias; (b) MSE.

the APES method fails to resolve the two closely spaced targets at $\theta_2 = -25^\circ$ and $\theta_3 = -21^\circ$. On the other hand, Capon gives well-resolved peaks around the target locations, but its amplitude estimates are significantly biased downward. On the basis of the GLR in Fig. 1.5d, the false peak due to the strong jammer can be readily rejected. Once again CAPES and CAML outperform the other methods and provide quite accurate target parameter estimates. To illustrate the improvement of CAML over CAPES for target amplitude estimation, we consider the amplitude estimation performance of Capon, CAPES, and CAML as a function of SNR. All the other simulation parameters are the same as in Fig. 1.5. Figures 1.6a,b show, respectively, the bias and mean-squared error (MSE) of the amplitude estimate for the target

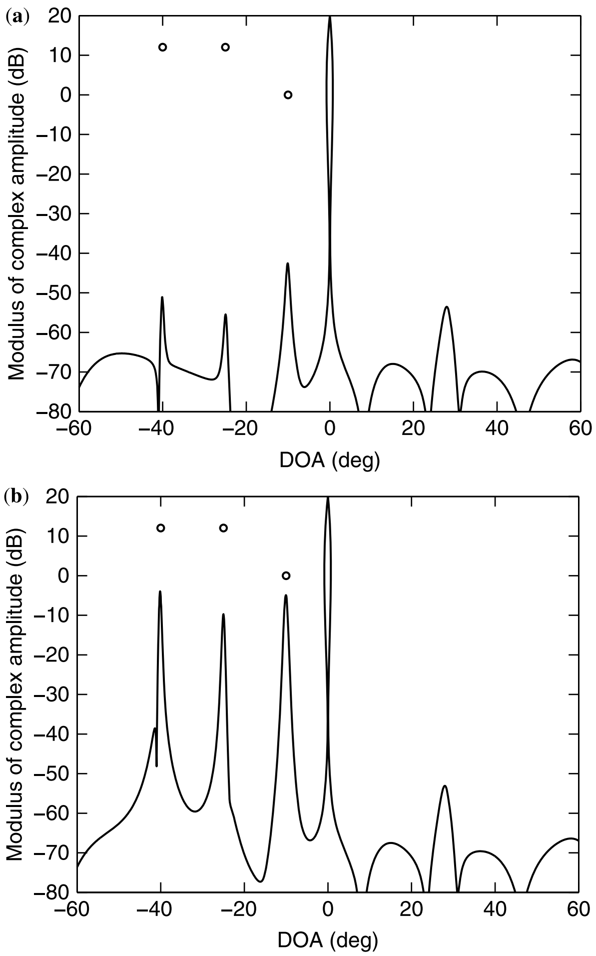

Figure 1.7 Spatial spectral estimates in the presence of array calibration errors, when $\theta_1 = -40^\circ$, $\theta_2 = -25^\circ$, and $\theta_3 = -10^\circ$: (a) Capon; (b) APES; (c) RCB with $\epsilon_r = 0.1$; (d) DCRCB with $\epsilon_r = 0.1$.

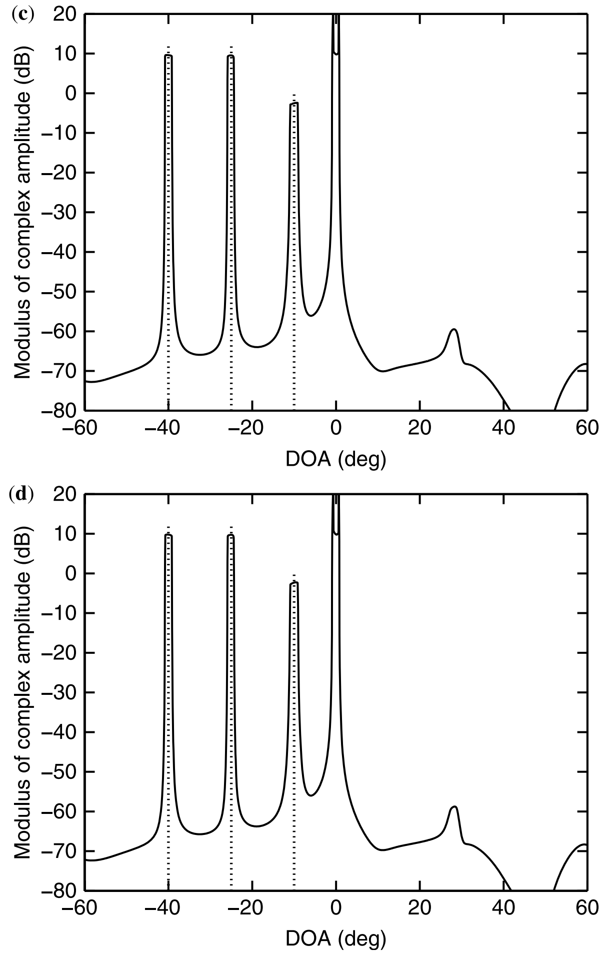

Figure 1.7 *Continued.*

at θ_3. The results are obtained using 1000 Monte Carlo simulations. As seen from these figures, the Capon estimate is biased downward significantly. Because of this bias, an error floor occurs in the MSE of the Capon estimate. CAPES is also biased downward at very low SNR. The CAML estimator is unbiased and outperforms CAPES for the entire range of the SNR considered, especially at low SNR.

We next consider the case where array calibration errors are present. To simulate the array calibration error, each element of the steering vector $\mathbf{a}(\theta) = \mathbf{b}(\theta)$, for each incident signal, is perturbed with a zero-mean circularly symmetric complex Gaussian random variable with variance 0.005 and then scaled to have norm $\sqrt{M_r}$, so that the squared Euclidean norm of the difference between the true array steering vector and the presumed one is about 0.05. We let $\mathrm{SNR} = 30\,\mathrm{dB}$. The other simulation parameters are the same as those in Fig. 1.4. For the sake of description convenience, the moduli of the amplitude estimates, that is, the y axes of Figs. 1.7a–d, are on a dB scale. As shown in Fig. 1.7a, the Capon method fails to work properly in the presence of array calibration errors, as expected: its amplitude estimates at the target locations are severely biased downward (by >60 dB for some of them). Although APES gives much better performance than Capon, its amplitude estimates at the target locations are ~ 10 dB lower than the true amplitudes. On the other hand, both RCB and DCRCB provide accurate estimates of the target amplitudes as well as target locations, but their peaks are wider (and hence their resolutions

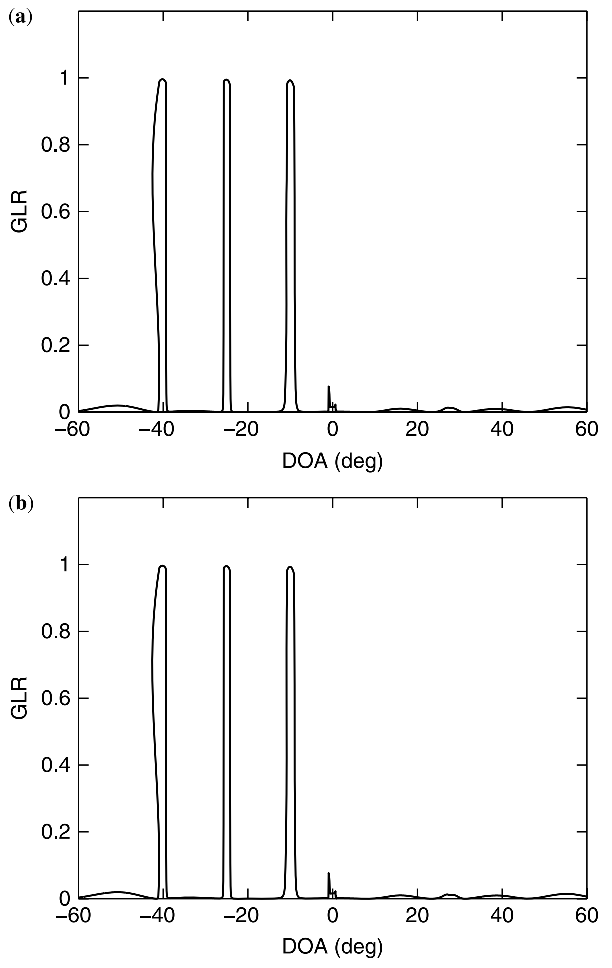

Figure 1.8 GLRs and refined spatial spectral estimates in the presence of array calibration errors, when $\theta_1 = -40^\circ$, $\theta_2 = -25^\circ$, and $\theta_3 = -10^\circ$: (a) GLR of RCB; (b) GLR of DCRCB; (c) refined spatial spectral estimate of RCB; (d) refined spatial spectral estimate of DCRCB.

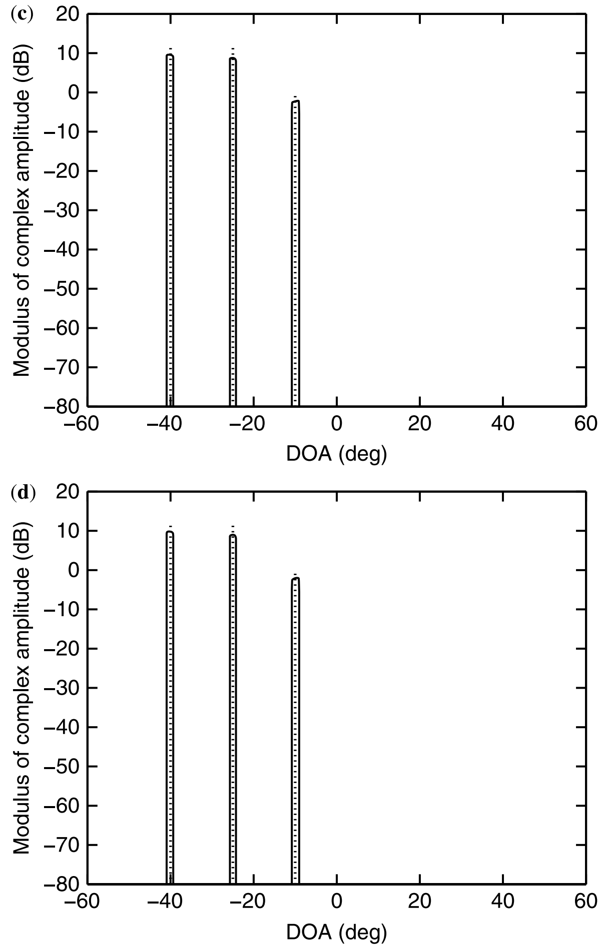

Figure 1.8 *Continued.*

are poorer) compared to what is shown in Fig. 1.4b, as expected (robustness to array calibration errors inherently reduces the resolution).

Figures 1.8a,b show the GLRs corresponding to RCB and DCRCB, as functions of θ, which are obtained by replacing $\mathbf{b}(\theta)$ in (1.61) by $\hat{\mathbf{b}}(\theta)$ and $\hat{\hat{\mathbf{b}}}(\theta)$ from Sections 1.4.2.1 and 1.4.2.2, respectively. As we can see, both RCB and DCRCB give high GLRs at the target locations and a low GLR at the jammer location. From the GLRs, we can again readily and correctly estimate the number of targets to be 3. Plotting the spatial spectral estimates in Figs. 1.7c,d only for the angles at which the corresponding GLRs are above a given threshold (say, 0.8), we obtain the refined spatial spectral estimates in Figs. 1.8c,d. These refined spatial spectral estimates obtained by RCB and DCRCB provide an accurate description of the target scenario.

1.5 PARAMETRIC TECHNIQUES FOR PARAMETER ESTIMATION

Several nonparametric data adaptive target parameter estimation methods for MIMO radar with collocated antennas have been presented in Section 1.4. We now consider parametric techniques for target parameter estimation as well as target number detection for MIMO radar with collocated antennas. Cyclic optimization algorithms are presented to obtain the maximum-likelihood (ML) estimates of the target parameters, and a Bayesian information criterion (BIC) is used for target number detection. Specifically, an approximate cyclic optimization (ACO) approach is first presented, which maximizes the likelihood function approximately. Then an exact cyclic optimization (ECO) approach that maximizes the exact likelihood function is introduced for target parameter estimation. The ACO and ECO target parameter estimates are used with the BIC for target number determination.

To remind the reader with some notation, we assume that the number of targets in a particular range and Doppler bin is K. The received data matrix can be written as

$$\mathbf{Y} = \sum_{k=1}^{K} \mathbf{b}^c(\theta_k)\beta_k \mathbf{s}^T(\theta_k) + \tilde{\mathbf{Z}}, \quad \text{with} \quad \mathbf{s}^T(\theta_k) = \mathbf{a}^*(\theta_k)\mathbf{X} \tag{1.62}$$

where the parameters are defined similarly as in (1.6) and (1.46), and the column of $\tilde{\mathbf{Z}} \in \mathbb{C}^{M_r \times N}$ comprise independently and identically distributed (i.i.d.) circularly symmetric complex Gaussian random vectors with mean zero and unknown covariance matrix $\mathbf{Q}$. Our goal here is to detect the unknown target number K and estimate the unknown target location parameters $\{\theta_k\}_{k=1}^K$ as well as complex amplitudes $\{\beta_k\}_{k=1}^K$.

1.5.1 ML and BIC

Consider first the ML estimation of the target parameters $\{\beta_k\}_{k=1}^K$ and $\{\theta_k\}_{k=1}^K$ by assuming that the target number K is known *a priori*. The BIC estimate of the unknown K is described later.

The negative loglikelihood function (LF) of $\{\theta_k\}_{k=1}^K$, $\{\beta_k\}_{k=1}^K$, and the unknown elements in $\mathbf{Q}$ for the data model in (1.62) can be written, to within a constant, as

$$\begin{aligned} f_1(\mathbf{Q}, \{\theta_k\}, \{\beta_k\}) = N \ln(|\mathbf{Q}|) & \\ + \operatorname{tr}\Bigg\{ \Bigg[\mathbf{Y} - \sum_{k=1}^{K} \mathbf{b}^c(\theta_k)\beta_k \mathbf{s}^T(\theta_k)\Bigg] & \\ \times \Bigg[\mathbf{Y} - \sum_{k=1}^{K} \mathbf{b}^c(\theta_k)\beta_k \mathbf{s}^T(\theta_k)\Bigg]^* \mathbf{Q}^{-1} \Bigg\} & \end{aligned} \tag{1.63}$$

where $|\cdot|$ and $\operatorname{tr}(\cdot)$ denote the determinant and trace of a matrix, respectively.

The minimization of the negative loglikelihood function in (1.63) with respect to $\mathbf{Q}$ yields the following concentrated negative log-LF of the unknown parameters $\{\theta_k, \beta_k\}$:

$$f_2(\{\theta_k\}, \{\beta_k\}) = N \ln \left| \left[\mathbf{Y} - \sum_{k=1}^{K} \mathbf{b}^c(\theta_k)\beta_k \mathbf{s}^T(\theta_k) \right] \times \left[\mathbf{Y} - \sum_{k=1}^{K} \mathbf{b}^c(\theta_k)\beta_k \mathbf{s}^T(\theta_k) \right]^* \right| \tag{1.64}$$

The minimization of this cost function must be conducted with respect to $3K$ unknown real-valued variables $\{\theta_k\}_{k=1}^K$ and the real and imaginary parts of $\{\beta_k\}_{k=1}^K$. Because this optimization problem does not appear to admit a closed-form solution, we present two cyclic optimization algorithms for target parameter estimation in the following.

The estimates of the target parameters $\{\beta_k\}_{k=1}^K$ and $\{\theta_k\}_{k=1}^K$ are associated with the assumed target number K. Once we got the estimates of $\{\beta_k\}_{k=1}^K$ and $\{\theta_k\}_{k=1}^K$ for various values of K, the target number K can be detected by minimizing the following BIC cost function (see, e.g., Ref. 55)

$$\mathrm{BIC}(K) = 2f_2(\{\hat{\theta}_k\}_{k=1}^K, \{\hat{\beta}_k\}_{k=1}^K) + 3K \ln N \tag{1.65}$$

where $\hat{\theta}_k$ and $\hat{\beta}_k$ are the estimates of θ_k and β_k, respectively.

1.5.1.1 ACO ACO can be used to obtain initial target parameter estimates, which can be refined via ECO. The received data matrix in (1.62) can be rewritten in the form of the diagonal growth curve (DGC) model [46]. Using the AML estimator in [83], we can then obtain an estimate of $\{\beta_k\}_{k=1}^K$ that can be used to further concentrate the negative log-LF in (1.64), at least approximately.

For convenience, let

$$\mathbf{B}_r(\boldsymbol{\theta}) = [\mathbf{b}^c(\theta_1) \ \cdots \ \mathbf{b}^c(\theta_K)] \tag{1.66}$$

$$\mathbf{S}(\boldsymbol{\theta}) = [\mathbf{s}(\theta_1) \ \cdots \ \mathbf{s}(\theta_K)]^T \tag{1.67}$$

and

$$\boldsymbol{\theta} = [\theta_1 \ \cdots \ \theta_K]^T \tag{1.68}$$

Then, (1.64) can be rewritten as

$$f(\boldsymbol{\beta}, \boldsymbol{\theta}) = N \ln \left| [\mathbf{Y} - \mathbf{B}_r \operatorname{diag}(\boldsymbol{\beta})\mathbf{S}][\mathbf{Y} - \mathbf{B}_r \operatorname{diag}(\boldsymbol{\beta})\mathbf{S})]^* \right| \tag{1.69}$$

where $\boldsymbol{\beta}$ is as defined in (1.11). By using the AML estimator [46], we can estimate $\boldsymbol{\beta}$ approximately, for any fixed vector θ, as follows

$$\hat{\boldsymbol{\beta}}_{\mathrm{AML}} = [(\mathbf{B}_r^* \tilde{\mathbf{Q}}^{-1} \mathbf{B}_r) \odot (\mathbf{S}^c \mathbf{S}^T)]^{-1} \operatorname{vecd}(\mathbf{B}_r^* \tilde{\mathbf{Q}}^{-1} \mathbf{Y}\mathbf{S}^*) \tag{1.70}$$

where

$$\tilde{\mathbf{Q}} = \hat{\mathbf{R}}_{yy} - \frac{1}{N}\mathbf{Y}\mathbf{S}^*(\mathbf{S}\mathbf{S}^*)^{-1}\mathbf{S}\mathbf{Y}^* \tag{1.71}$$

and $\hat{\mathbf{R}}_{yy}$ is given as in (1.31). Note that (1.70) is similar to (1.47). Note also that for notational convenience we have omitted the argument $\boldsymbol{\theta}$ of $\mathbf{B}_r$, $\mathbf{S}$, and $\tilde{\mathbf{Q}}$ in (1.70). Substituting (1.70) in (1.69), followed by some straightforward manipulations, yields the concentrated approximate negative log-LF of $\boldsymbol{\theta}$ as follows:

$$\begin{aligned} f_3(\boldsymbol{\theta}) = {} & N\ln|\tilde{\mathbf{Q}}| + N\ln\Big\{1 - M_r + \mathrm{tr}(\tilde{\mathbf{Q}}^{-1}\hat{\mathbf{R}}_{yy}) \\ & - \frac{1}{N}\mathrm{vecd}^*(\mathbf{B}_r^*\tilde{\mathbf{Q}}^{-1}\mathbf{Y}\mathbf{S}^*) \\ & \times [(\mathbf{B}_r^*\tilde{\mathbf{Q}}^{-1}\mathbf{B}_r) \odot (\mathbf{S}^c\mathbf{S}^T)]^{-1}\mathrm{vecd}(\mathbf{B}_r^*\tilde{\mathbf{Q}}^{-1}\mathbf{Y}\mathbf{S}^*)\Big\} \end{aligned} \tag{1.72}$$

Note that by using AML, the number of unknowns in (1.72) has been reduced to K. Cyclic optimization (CO) techniques can be used to minimize (1.72) with respect to $\{\theta_k\}_{k=1}^K$. Within each substep of the CO algorithm, we estimate one target location parameter, say, θ_k, by using the most recent estimates of the other parameters. The iteration of the CO algorithm is terminated when "practical convergence" is reached, which may be determined by checking whether the relative change of the log-LF between two consecutive iterations is less than some predetermined threshold ϵ_t. The ACO algorithm can be described as follows:

Step 0: Initialization. Set $i = 1$.

Step 1: Cyclic Optimization:

(a) Do the following until "practical convergence" is reached. For $k =$ i, 1, 2, ..., $i - 1$ estimate θ_k by searching the minimum of the cost function (1.72) using the most recent estimates of $\{\theta_p\}^i_{p\neq k,\, p=1}$.

(b) Set $i = i + 1$ and go to step 2(a) until i reaches a prescribed maximum number.

Step 2: BIC Order Selection. Find the minimum of $\mathrm{BIC}(i) = 2f_2(\hat{\theta}^i) + 3i\ln N$ with respect to i.

The so-obtained i corresponding to the minimum of BIC(i) is the estimate of target number K, and the corresponding $\{\hat{\theta}_k\}$ are the estimates of the target location parameters with $\hat{\theta}^i = \{\hat{\theta}_k\}_{k=1}^i$. Once $\hat{\theta}^i$ has been determined, the corresponding $\hat{\beta}$ can be obtained by using (1.70).

1.5.1.2 ECO Inspired by the RELAX method [56], ECO determines the parameters of each target iteratively. At each step, ECO estimates the parameters of one target by assuming that the other target parameters are given. Let

$$\tilde{\mathbf{Y}}_k = \mathbf{Y} - \sum_{p \neq k} \mathbf{b}^c(\hat{\theta}_p)\hat{\beta}_p \mathbf{s}^T(\hat{\theta}_p) \tag{1.73}$$

Then, the cost function in (1.64) reduces to

$$f(\theta_k, \beta_k) = N \ln \left| [\tilde{\mathbf{Y}}_k - \beta_k \mathbf{b}^c(\theta_k)\mathbf{s}^T(\theta_k)][\tilde{\mathbf{Y}}_k - \beta_k \mathbf{b}^c(\theta_k)\mathbf{s}^T(\theta_k)]^* \right| \tag{1.74}$$

Minimizing (1.74) with respect to β_k yields

$$\hat{\beta}_k = \frac{\mathbf{b}^T(\theta_k)\tilde{\mathbf{Q}}_k^{-1}\tilde{\mathbf{Y}}_k \mathbf{s}^c(\theta_k)}{\mathbf{b}^T(\theta_k)\tilde{\mathbf{Q}}_k^{-1}\mathbf{b}^c(\theta_k)\, \|\mathbf{s}(\theta_k)\|^2} \tag{1.75}$$

where $\|\cdot\|$ denotes the Euclidean norm, and

$$\tilde{\mathbf{Q}}_k(\theta_k) = \hat{\mathbf{R}}_k - \frac{\tilde{\mathbf{Y}}_k\, \mathbf{s}^c(\theta_k)\mathbf{s}^T(\theta_k)\tilde{\mathbf{Y}}_k^*}{N\, \|\mathbf{s}(\theta_k)\|^2} \tag{1.76}$$

and where

$$\hat{\mathbf{R}}_k = \frac{\tilde{\mathbf{Y}}_k \tilde{\mathbf{Y}}_k^*}{N}. \tag{1.77}$$

Inserting (1.75) into (1.74) and after some matrix manipulations (see, e.g., Ref. 30), we obtain the following concentrated negative log-LF function of θ_k:

$$f(\theta_k) = N \ln |\hat{\mathbf{R}}_k| + N \ln [\mathbf{b}^T(\theta_k)\hat{\mathbf{R}}_k^{-1}\mathbf{b}^c(\theta_k)] - N \ln [\mathbf{b}^T(\theta_k)\tilde{\mathbf{Q}}_k^{-1}\mathbf{b}^c(\theta_k)] \tag{1.78}$$

Then, θ_k can be estimated by searching for the minimum of (1.78), and β_k can be estimated by substituting the so-obtained $\hat{\theta}_k$ into (1.75).

Combining BIC and ACO with a RELAX-type procedure [56], whose main step is as described above, leads to ECO, which can be summarized as follows:

Step 0: Initialization. Set $i = 1$.

Step 1: Cyclic Optimization:

(a) Obtain initial parameter estimates of $\{\theta_k\}_{k=1}^i$ and $\{\beta_k\}_{k=1}^i$ by running step 1(a) of ACO and Eq. (1.70).

(b) Do the following until "practical convergence" is reached. For $k = i, 1, 2, \ldots, i-1$.

Compute $\tilde{\mathbf{Y}}_k$ in (1.73) by using the most recent estimates of $\{\beta_p\}_{p \neq k, p=1}^i$ and $\{\theta_p\}_{p \neq k, p=1}^i$.

Estimate θ_k by searching for the minimum of the cost function in (1.78);

Estimate β_k by inserting the so-obtained $\hat{\theta}_k$ in (1.75).

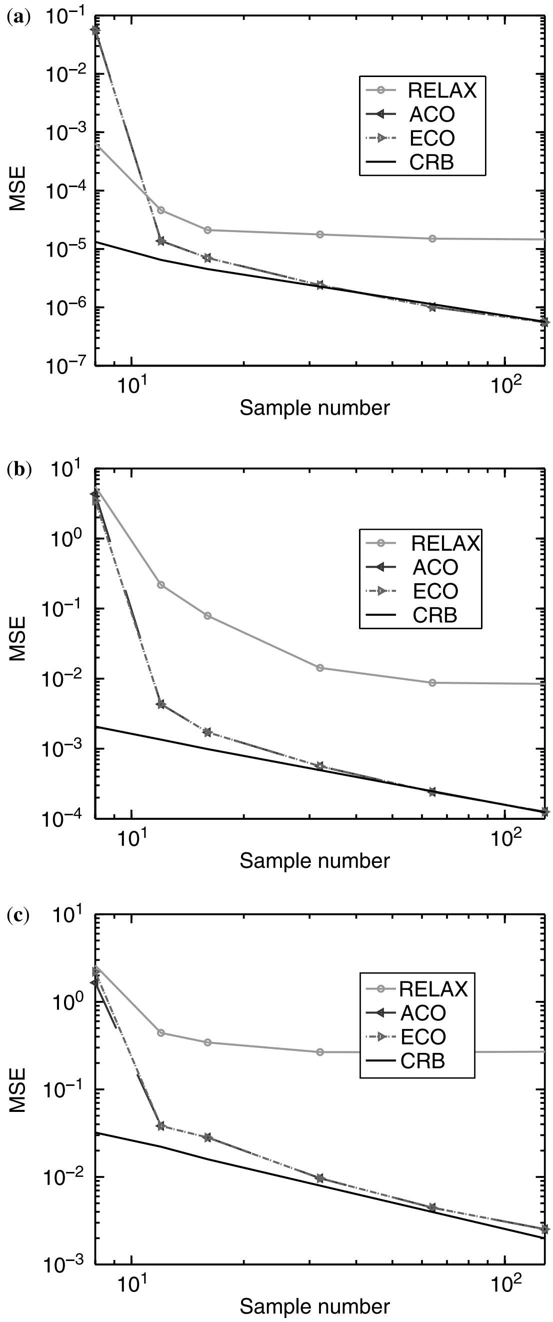

Figure 1.9 Empirical MSEs of the estimates of target location and amplitude parameters versus the number of data samples when SNR = 20 dB: (a) θ_1; (b) θ_2; (c) θ_3; (d) β_1; (e) β_2; (f) β_3.

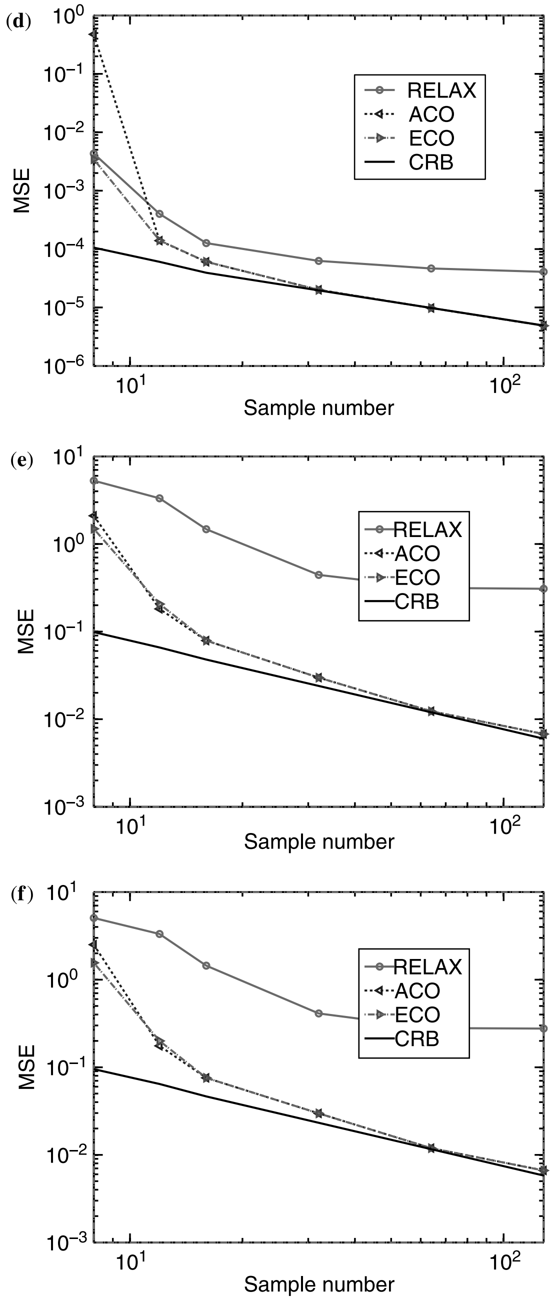

Figure 1.9 *Continued.*

(c) Compute BIC(i) using (1.65), and the so-obtained $\{\hat{\beta}_k\}_{k=1}^{i}$ and $\{\hat{\theta}_k\}_{k=1}^{i}$.

(d) Set $i = i + 1$ and go to step 1(a) until i reaches a prescribed maximum number.

Step 2: BIC Order Selection. Find the minimum of the so-obtained BIC(i) with respect to i.

1.5.2 Numerical Examples

Consider a MIMO radar system where uniform linear arrays with $M_t = M_r = 5$ antennas are used for both transmitting and receiving. The interelement spacing is 0.5λ for the receive array and 2.5λ for the transmit array. The transmitted waveforms are orthogonal QPSK sequences that satisfy $\hat{\mathbf{R}}_{xx} \triangleq (1/N)\mathbf{X}\mathbf{X}^* = \mathbf{I}$ [see also (1.28)].

Consider a scenario in which $K = 3$ targets are at $\theta_1 = -20^\circ$, $\theta_2 = -10^\circ$, and $\theta_3 = -9^\circ$ with the corresponding complex amplitudes $\beta_1 = 4$, $\beta_2 = 4$, and $\beta_3 = 1$, respectively. There is a strong jammer at 0° with an unknown waveform and with amplitude 100 (i.e., 40 dB stronger than β_3). The received signal is corrupted by a zero-mean spatially colored Gaussian noise with an unknown covariance matrix. The (p,q)th element of the noise covariance matrix is $(1/\text{SNR})\, 0.9^{|p-q|} e^{j[(p-q)\pi]/2}$. We choose the "practical convergence" threshold as $\epsilon_t = 10^{-6}$.

We first determine the empirical mean-squared errors (MSEs) of the target location and amplitude parameters estimated by ACO and ECO, as functions of the number of data samples, when the number of targets is assumed to be known *a priori*. For comparison purposes, we also give the performance of a RELAX algorithm, which is essentially a simplified version of ECO without the initialization step, namely, step 1(a). We also provide the corresponding Cramér–Rao bounds (CRBs) (see, e.g., Ref. 30), which represent the best possible performance of any unbiased estimators. The empirical MSEs are all obtained by 100 Monte Carlo simulations. From Figs. 1.9a–f, we can see that RELAX suffers from an error floor problem. ACO and

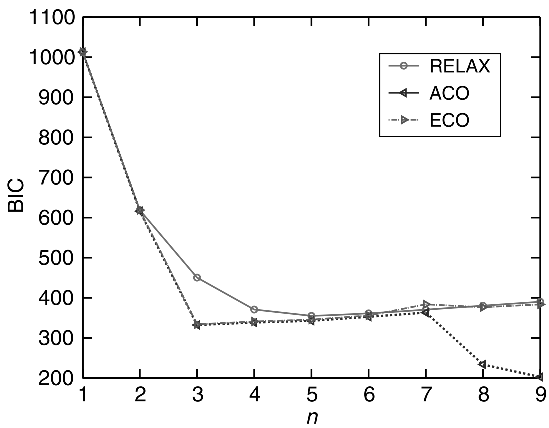

Figure 1.10 BIC cost functions obtained by RELAX, ACO, and ECO when $N = 32$ and SNR = 20 dB.

ECO outperform RELAX significantly. Their MSEs approach the CRB as the number of data samples increases. At a small number of data samples, ECO can provide slightly better performance than does ACO.

Figure 1.10 shows the BIC cost function obtained by RELAX, ACO, and ECO in one of the Monte Carlo simulations when $N = 32$ and SNR = 20 dB. As shown, ECO can be used with BIC to correctly detect the target number, while RELAX and ACO fail to work properly. In fact, ECO detected the target number accurately in all 100 Monte Carlo simulations.

1.6 TRANSMIT BEAMPATTERN DESIGNS

The probing signal vector transmitted by a MIMO radar system can be designed to approximate a desired transmit beampattern and also to minimize the cross-correlation of the signals bounced from various targets of interest — an operation that, like the direct application of adaptive techniques, would be hardly possible for a phased-array radar [12,13,17,23].

The power of the probing signal at a generic focal point with location θ is given by [see (1.1)]

$$P(\theta) = \mathbf{a}^*(\theta)\mathbf{R}\mathbf{a}(\theta) \tag{1.79}$$

where $\mathbf{R}$ is the covariance matrix of $\mathbf{x}(n)$:

$$\mathbf{R} = E\{\mathbf{x}(n)\mathbf{x}^*(n)\} \tag{1.80}$$

The "spatial spectrum" in (1.79), as a function of θ, will be called the *transmit beampattern*.

We assume in this section that the transmit and receive antennas are identically located [$\mathbf{b}(\theta) = \mathbf{a}(\theta)$]. The received data vector in (1.6) can then be expressed as

$$\mathbf{y}(n) = \sum_{k=1}^{K} \beta_k \mathbf{a}^c(\theta_k)\mathbf{a}^*(\theta_k)\mathbf{x}(n) + \boldsymbol{\epsilon}(n), \quad n = 1, \ldots, N \tag{1.81}$$

1.6.1 Beampattern Matching Design

The first problem we will consider in this subsection consists of choosing $\mathbf{R}$, under a uniform elemental power constraint

$$R_{mm} = \frac{c_p}{M_t}, \quad m = 1, \ldots, M_t; \quad \text{with } c_p \text{ given} \tag{1.82}$$

where R_{mm} denotes the (m, m)th element of $\mathbf{R}$, to achieve the following goals [17,23]:

1. Control the spatial power at a number of given target locations by matching (or approximating) a desired transmit beampattern.

2. Minimize the cross-correlation between the probing signals at a number of given target locations; note from (1.1) that the cross-correlation between the probing signals at locations θ and $\bar{\theta}$ is given by $\mathbf{a}^*(\theta)\mathbf{R}\mathbf{a}(\bar{\theta})$.

Let $\phi(\theta)$ denote a desired transmit beampattern, and let $\{\mu_l\}_{l=1}^{L}$ be a fine grid of points that cover the location sectors of interest. We assume that some of these grid-points are good approximations of the locations $\{\theta_k\}_{k=1}^{\tilde{K}}$ of the targets of interest, and that we dispose of (initial) estimates $\{\hat{\theta}_k\}_{k=1}^{\tilde{K}}$ of $\{\theta_k\}_{k=1}^{\tilde{K}}$, where $\tilde{K}$ denotes the number of targets of interest that we wish to probe further. We can obtain $\phi(\theta)$ and $\{\hat{\theta}_k\}_{k=1}^{\tilde{K}}$, for instance, using the Capon and GLRT approaches presented in Section 1.4.

As stated above, our goal is to choose $\mathbf{R}$ such that the transmit beampattern, $\mathbf{a}^*(\theta)\mathbf{R}\mathbf{a}(\theta)$, matches or rather approximates [in a least-squares (LS) sense] the desired transmit beampattern, $\phi(\theta)$, over the sectors of interest, and also such that the cross-correlation (beam)pattern, $\mathbf{a}^*(\theta)\mathbf{R}\mathbf{a}(\bar{\theta})$ (for $\theta \neq \bar{\theta}$), is minimized (once again, in a LS sense) over the set $\{\hat{\theta}_k\}_{k=1}^{\tilde{K}}$. Mathematically, we want to solve the following problem

$$\min_{\alpha,\mathbf{R}} \left\{ \frac{1}{L}\sum_{l=1}^{L} w_l[\alpha\phi(\mu_l) - \mathbf{a}^*(\mu_l)\mathbf{R}\mathbf{a}(\mu_l)]^2 \right.$$
$$\left. + \frac{2w_c}{\tilde{K}^2 - \tilde{K}} \sum_{k=1}^{\tilde{K}-1} \sum_{p=k+1}^{\tilde{K}} \left|\mathbf{a}^*(\hat{\theta}_k)\mathbf{R}\mathbf{a}(\hat{\theta}_p)\right|^2 \right\}$$

subject to

$$\begin{aligned} R_{mm} &= \frac{c_p}{M_t}, \quad m = 1, \ldots, M_t \\ \mathbf{R} &\geq 0 \end{aligned} \tag{1.83}$$

where α is a scaling factor, $w_l \geq 0$, $l = 1, \ldots, L$, is the weight for the lth gridpoint, and $w_c \geq 0$ is the weight for the cross-correlation term. The reason for introducing α in the design problem is that typically $\phi(\theta)$ is given in a "normalized form" [e.g., satisfying $\phi(\theta) \leq 1$, $\forall\theta$], and our interest lies in approximating an appropriately scaled version of $\phi(\theta)$, not $\phi(\theta)$ itself. The value of w_l should be larger than that of w_k if the beampattern matching at μ_l is considered to be more important than the matching at μ_k. Note that by choosing $\max_l w_l > w_c$ we can give more weight to the first term in the design criterion above, and vice versa for $\max_l w_l < w_c$. We have shown [17,23] (see also below) that this design problem can be efficiently solved in polynomial time as a semidefinite quadratic program (SQP).

Let vec($\mathbf{R}$) denote the $M_t^2 \times 1$ vector obtained by stacking the columns of $\mathbf{R}$ on top of each other. Let $\mathbf{r}_v$ denote the $M_t^2 \times 1$ real-valued vector made from

R_{mm} $(m = 1, \ldots, M_t)$ and the real and imaginary parts of R_{mp}, $(m, p = 1, \ldots, M_t; p > m)$. Then, given the Hermitian symmetry of $\mathbf{R}$, we can write

$$\mathrm{vec}(\mathbf{R}) = \mathbf{J}\mathbf{r}_v \tag{1.84}$$

for a suitable $M_t^2 \times M_t^2$ matrix $\mathbf{J}$ whose elements are easily derived constants $(0, \pm j, \pm 1)$. Making use of (1.84) and of some simple properties of the vec operator, the reader can verify that (the symbol $\otimes$ denotes the Krönecker product operator):

$$\begin{aligned}\mathbf{a}^*(\mu_l)\mathbf{R}\mathbf{a}(\mu_l) &= \mathrm{vec}\,[\mathbf{a}^*(\mu_l)\mathbf{R}\mathbf{a}(\mu_l)] \\ &= [\mathbf{a}^T(\mu_l) \otimes \mathbf{a}^*(\mu_l)]\mathbf{J}\mathbf{r}_v \\ &\triangleq -\mathbf{g}_l^T\mathbf{r}_v\end{aligned} \tag{1.85}$$

$$\begin{aligned}\mathbf{a}^*(\hat{\theta}_k)\mathbf{R}\mathbf{a}(\hat{\theta}_p) &= [\mathbf{a}^T(\hat{\theta}_p) \otimes \mathbf{a}^*(\hat{\theta}_k)]\mathbf{J}\mathbf{r}_v \\ &\triangleq \mathbf{d}_{k,p}^*\mathbf{r}_v\end{aligned} \tag{1.86}$$

Inserting (1.85) and (1.86) into (1.83) yields the following more compact form of the design criterion (which clearly shows the quadratic dependence on $\mathbf{r}_v$ and α)

$$\begin{aligned}&\frac{1}{L}\sum_{l=1}^{L} w_l\left[\alpha\phi(\mu_l) + \mathbf{g}_l^T\mathbf{r}_v\right]^2 + \frac{2w_c}{\tilde{K}^2 - \tilde{K}}\sum_{k=1}^{\tilde{K}-1}\sum_{p=k+1}^{\tilde{K}}\left|\mathbf{d}_{k,p}^*\mathbf{r}_v\right|^2 \\ &= \frac{1}{L}\sum_{l=1}^{L} w_l\left\{\begin{bmatrix}\phi(\mu_l) & \mathbf{g}_l^T\end{bmatrix}\begin{bmatrix}\alpha \\ \mathbf{r}_v\end{bmatrix}\right\}^2 \\ &\quad + \frac{2w_c}{\tilde{K}^2 - \tilde{K}}\sum_{k=1}^{\tilde{K}-1}\sum_{p=k+1}^{\tilde{K}}\left|\begin{bmatrix}0 & \mathbf{d}_{k,p}^*\end{bmatrix}\begin{bmatrix}\alpha \\ \mathbf{r}_v\end{bmatrix}\right|^2 \\ &\triangleq \boldsymbol{\rho}^T\boldsymbol{\Gamma}\boldsymbol{\rho}\end{aligned} \tag{1.87}$$

where

$$\boldsymbol{\rho} = \begin{bmatrix}\alpha \\ \mathbf{r}_v\end{bmatrix} \tag{1.88}$$

and

$$\begin{aligned}\boldsymbol{\Gamma} &= \frac{1}{L}\sum_{l=1}^{L} w_l\begin{bmatrix}\phi(\mu_l) \\ \mathbf{g}_l\end{bmatrix}\begin{bmatrix}\phi(\mu_l) & \mathbf{g}_l^T\end{bmatrix} \\ &\quad + \mathrm{Re}\left\{\frac{2w_c}{\tilde{K}^2 - \tilde{K}}\sum_{k=1}^{\tilde{K}-1}\sum_{p=k+1}^{\tilde{K}}\begin{bmatrix}0 \\ \mathbf{d}_{k,p}\end{bmatrix}\begin{bmatrix}0 & \mathbf{d}_{k,p}^*\end{bmatrix}\right\}\end{aligned} \tag{1.89}$$

where Re(·) denotes the real part. The matrix $\boldsymbol{\Gamma}$ above is usually rank-deficient. For example, in the case of an M_t sensor uniform linear array with half-wavelength (or smaller) interelement spacing and for $w_c = 0$, one can show that the rank of $\boldsymbol{\Gamma}$ is $2M_t$. The rank deficiency of $\boldsymbol{\Gamma}$, however, does not pose any serious problem for the SQP solver outlined below.

Making use of the form in (1.87) of the design criterion, we can rewrite (1.83) as the following SQP (see, e.g., Refs. 57 and 58)

$$\begin{aligned}
&\min_{\delta,\varrho} && \delta \\
&\text{subject to} && \|\varrho\| \leq \delta \\
& && R_{mm}(\varrho) = \frac{c_p}{M_t}, \qquad m = 1, \ldots, M_t \\
& && \mathbf{R}(\varrho) \geq 0
\end{aligned} \tag{1.90}$$

where ($\boldsymbol{\Gamma}^{1/2}$ denotes a Hermitian square root of $\boldsymbol{\Gamma}$)

$$\varrho = \boldsymbol{\Gamma}^{1/2}\boldsymbol{\rho} \tag{1.91}$$

and where we have indicated explicitly the (linear) dependence of $\mathbf{R}$ on ϱ.

In some applications, we would like the synthesized beampattern at some given locations to be very close to the desired values. As already mentioned, to a certain extent, this design goal can be achieved by the selection of the weights $\{w_l\}$ of the design criterion in (1.83). However, if we want the beampattern to match the desired values *exactly*, then selecting the weights $\{w_l\}$ is not enough, and we have to modify the design problem, as we now explain.

Consider, for instance, that we want the transmit beampattern at a number of points to be equal to certain desired levels. Then the optimization problem we need to solve is (1.83) with the following additional constraints

$$\mathbf{a}^*(\breve{\mu}_l)\mathbf{R}\mathbf{a}(\breve{\mu}_l) = \zeta_l, \quad l = 1, \ldots, \breve{L} \tag{1.92}$$

where $\{\zeta_l\}$ are predetermined levels. A similar modification of (1.83) takes place when the transmit beampattern at a number of points $\{\breve{\mu}_l\}_{l=1}^{\breve{L}}$ is restricted to be less than or equal to certain desired levels. The extended problems (with additional either equality or inequality constraints) are also SQPs, and therefore, similarly to (1.83), they can be solved efficiently using readily available software [57,58].

1.6.2 Minimum Sidelobe Beampattern Design

Another beampattern design problem we consider consists of choosing $\mathbf{R}$, under the uniform elemental power constraint in (1.82), to achieve the following goals [17,23]:

1. Minimize the sidelobe level in a prescribed region.
2. Achieve a predetermined 3 dB width of the mainbeam.

This problem can be formulated as follows (where s.t. denotes "subject to")

$$\begin{aligned}
\min_{t,\mathbf{R}} \quad & -t \\
\text{s.t.} \quad & \mathbf{a}^*(\theta_0)\mathbf{R}\mathbf{a}(\theta_0) - \mathbf{a}^*(\mu_l)\mathbf{R}\mathbf{a}(\mu_l) \geq t, \quad \forall \mu_l \in \Omega \\
& \mathbf{a}^*(\theta_1)\mathbf{R}\mathbf{a}(\theta_1) = 0.5\mathbf{a}^*(\theta_0)\mathbf{R}\mathbf{a}(\theta_0) \\
& \mathbf{a}^*(\theta_2)\mathbf{R}\mathbf{a}(\theta_2) = 0.5\mathbf{a}^*(\theta_0)\mathbf{R}\mathbf{a}(\theta_0) \\
& \mathbf{R} \geq 0 \\
& R_{mm} = \frac{c_p}{M_t}, \quad m = 1, \ldots, M_t
\end{aligned} \tag{1.93}$$

where $\theta_2 - \theta_1$ (with $\theta_2 > \theta_0$ and $\theta_1 < \theta_0$) determines the 3 dB width of the mainbeam and Ω denotes the sidelobe region of interest. As shown in Refs. 17 and 23, this minimum sidelobe beampattern design problem can be efficiently solved in polynomial time as a semidefinite program (SDP). Note that we can relax somewhat the constraints in (1.93) defining the 3 dB width of the mainbeam; for instance, we can replace them by $(0.5 - \delta)\mathbf{a}^*(\theta_0)\mathbf{R}\mathbf{a}(\theta_0) \leq \mathbf{a}^*(\theta_i)\mathbf{R}\mathbf{a}(\theta_i) \leq (0.5 + \delta)\mathbf{a}^*(\theta_0)\mathbf{R}\mathbf{a}(\theta_0)$, $i = 1,2$, for some small δ. Such a relaxation leads to a design with lower sidelobes, and to an optimization problem that is feasible more often than (1.93).

We can also introduce some flexibility in the elemental power constraint by allowing the elemental power to be within a certain range around c_p/M_t, while still maintaining the same total transmit power of c_p. Such a relaxation of the design problem allows lower sidelobe levels and smoother beampatterns, as we will show later via some numerical examples.

1.6.3 Phased-Array Beampattern Design

Finally, consider the conventional phased-array beampattern design problem in which only the array weight vector can be adjusted and therefore all antennas transmit the same differently scaled waveform. We can readily modify the previously described beampattern matching or minimum sidelobe beampattern designs for the case of phased arrays by adding the constraint

$$\text{rank}(\mathbf{R}) = 1 \tag{1.94}$$

However, because of the rank 1 constraint, both these originally convex optimization problems become nonconvex. The lack of convexity makes the rank 1–constrained problems much harder to solve than the original convex optimization problems [59]. Semidefinite relaxation (SDR) is often used to obtain approximate solutions to such rank-constrained optimization problems [58]. Typically, the SDR is obtained by omitting the rank constraint. Hence, interestingly, *the MIMO beampattern design problems are SDRs of the corresponding phased-array beampattern design problems*.

In the numerical examples below, we have used the Newton-like algorithm presented in Ref. 59 to solve the rank 1–constrained design problems for phased arrays. This algorithm uses SDR to obtain an initial solution. Although the convergence of the said Newton-like algorithm is not guaranteed [59], we did not encounter any apparent problem in our numerical simulations. An interesting detail here is that the approach in Ref. 59 is for real-valued vectors and matrices; therefore we had to rewrite the rank 1 constraint in (1.94) in terms of real-valued quantities

$$\operatorname{rank}(\tilde{\mathbf{R}}) = 2 \tag{1.95}$$

where

$$\tilde{\mathbf{R}} = \begin{bmatrix} \operatorname{Re}\{\mathbf{R}\} & -\operatorname{Im}\{\mathbf{R}\} \\ \operatorname{Im}\{\mathbf{R}\} & \operatorname{Re}\{\mathbf{R}\} \end{bmatrix} \tag{1.96}$$

where $\operatorname{Re}\{\mathbf{x}\}$ and $\operatorname{Im}\{\mathbf{x}\}$ denote the real and imaginary parts of $\mathbf{x}$, respectively. The equivalence between (1.94) and (1.95) is proved in Appendix 1B.

1.6.4 Numerical Examples

We present several numerical examples to demonstrate the merits of the probing signal designs for MIMO radar systems. We consider a MIMO radar with a uniform linear array (ULA) constituting $M_t = M_r = M = 10$ antennas with half-wavelength spacing between adjacent antennas. This array is used both for transmitting and for receiving. Without loss of generality, the total transmit power is set to $c_p = 1$.

1.6.4.1 Beampattern Matching Design Consider first a scenario where $K = 3$ targets are located at $\theta_1 = -40^\circ$, $\theta_2 = 0^\circ$, and $\theta_3 = 40^\circ$ with complex amplitudes equal to $\beta_1 = \beta_2 = \beta_3 = 1$. There is a strong jammer at 25° with an unknown waveform (uncorrelated with the transmitted MIMO radar waveforms) with a power equal to 10^6 (60 dB). Each transmitted signal pulse has $N = 256$ samples. The received signal is corrupted by zero-mean circularly symmetric spatio temporally white Gaussian noise with variance σ^2. We assume that only the targets reflect the transmitted signals. In practice, the background can also reflect the signals. In the latter case, transmitting most of the power toward the targets should generate much less clutter returns than when transmitting power omnidirectionally. Therefore, a MIMO radar system with a proper transmit beampattern design might provide even greater performance gains than those demonstrated here.

Since we do not assume any prior knowledge about the target locations, orthogonal waveforms are used for MIMO probing. (We refer to this as “initial probing,” since after we get the target location estimates with this probing, we can optimize the transmitted beampattern to improve the estimation accuracy.) Using the data collected as a result of this initial probing, we can obtain the Capon spatial spectrum and the GLRT function (see Ref. 28 and Section 1.4). An example of the Capon spectrum for $\sigma^2 = -10$ dB is shown in Fig. 1.11a, where

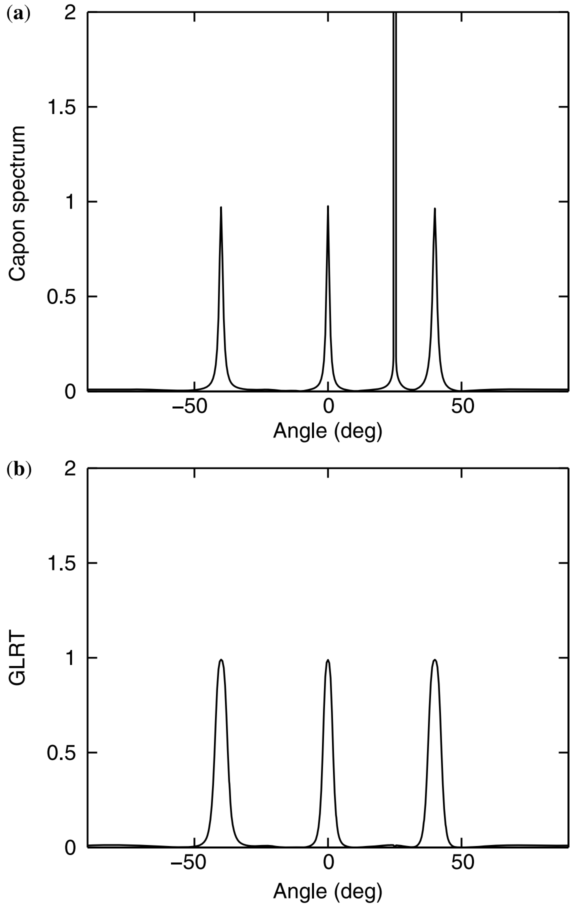

Figure 1.11 The Capon spatial spectrum and the GLRT pseudospectrum as functions of θ, for the initial omnidirectional probing: (a) Capon; (b) GLRT.

very narrow peaks occur around the target locations. Note that in Fig. 1.11a, a false peak occurs around $\theta = 25^\circ$, due to the presence of the very strong jammer. The corresponding GLRT pseudospectrum as a function of θ is shown in Fig. 1.11b. Note that the GLRT is close to one at the target locations and close to zero at any other locations, including the jammer location. Therefore, the GLRT can be used to reject the jammer peak in the Capon spectrum. The remaining peak locations in the Capon spectrum can be taken as the estimated target locations.

To illustrate the beampattern matching design, consider the example considered in Fig. 1.11. The initial target location estimates obtained using Capon or GLRT can be used to derive a desired beampattern. In the following numerical examples, we form the desired beampattern by using the dominant peak locations of the GLRT pseudospectrum, denoted as $\hat{\theta}_1, \ldots, \hat{\theta}_{\hat{K}}$, as follows (where $\hat{K}$ is the resulting estimate of K, and $\tilde{K} = \hat{K}$)

$$\phi(\theta) = \begin{cases} 1, & \theta \in [\hat{\theta}_k - \Delta, \hat{\theta}_k + \Delta], \; k = 1, \ldots, \hat{K} \\ 0, & \text{otherwise} \end{cases} \tag{1.97}$$

where 2Δ is the chosen beamwidth for each target (Δ should be greater than the expected error in $\{\hat{\theta}_k\}$). Figure 1.12b is obtained using (1.97) with $\Delta = 5^\circ$ in the beampattern matching design in (1.83) along with a mesh grid size of 0.1°, $w_l = 1$, $l = 1, \ldots, L$, and either $w_c = 0$ or $w_c = 1$. Note that the designs obtained with $w_c = 1$ and with $w_c = 0$ are similar to one another. However, the cross-correlation

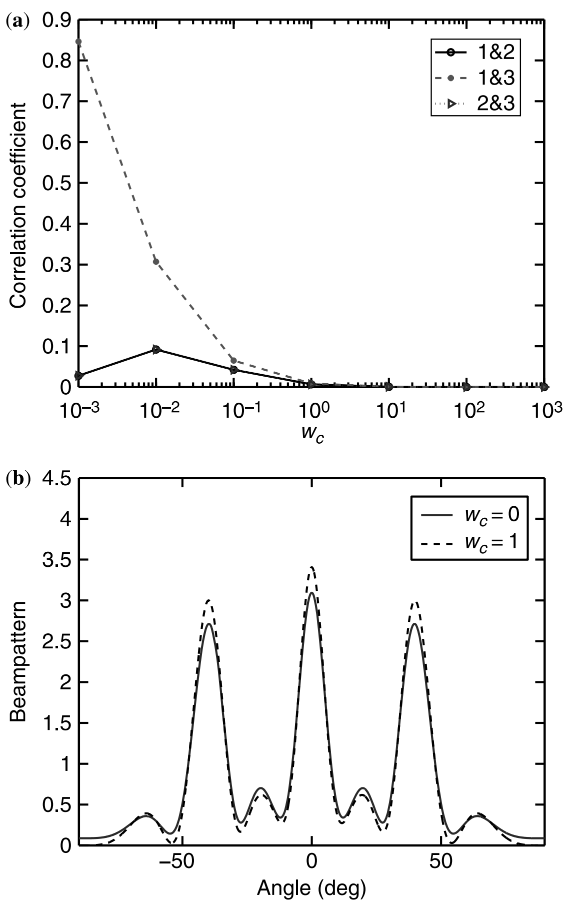

Figure 1.12 MIMO beampattern matching designs with $\Delta = 5^\circ$ and $c_p = 1$, under the uniform elemental power constraint: (a) cross-correlation coefficients of the three target reflected signals as functions of w_c; (b) comparison of the beampatterns obtained with $w_c = 0$ and $w_c = 1$.

behavior of the former is much better than that of the latter in that the reflected signal waveforms corresponding to using $w_c = 1$ are almost uncorrelated with each other, as shown in Fig. 1.12a.

In practice, the theoretical covariance matrix $\mathbf{R}$ of the transmitted signals is realized via the sample covariance matrix $\hat{\mathbf{R}}_{xx} = (1/N)\sum_{n=1}^{N} \mathbf{x}(n)\mathbf{x}^*(n)$, which may cause the synthesized transmit beampattern to be slightly different from the designed beampattern, unless $\hat{\mathbf{R}}_{xx} = \mathbf{R}$, which holds, for instance, if $\mathbf{x}(n) = \mathbf{R}^{1/2}\mathbf{w}(n)$ and $(1/N)\sum_{n=1}^{N} \mathbf{w}(n)\mathbf{w}^*(n) = \mathbf{I}$ exactly; in what follows, however, we assume that $\{\mathbf{w}(n)\}$ is a temporally and spatially white signal for which the last equality holds only approximately in finite samples. Let $\epsilon(\theta)$ denote the relative difference of the beampatterns obtained by using $\hat{\mathbf{R}}_{xx}$ and $\mathbf{R}$:

$$\epsilon(\theta) = \frac{\mathbf{a}^*(\theta)(\hat{\mathbf{R}}_{xx} - \mathbf{R})\mathbf{a}(\theta)}{\mathbf{a}^*(\theta)\mathbf{R}\mathbf{a}(\theta)}, \quad \theta \in [-90^\circ, 90^\circ] \tag{1.98}$$

Figure 1.13a shows an example of $\epsilon(\theta)$, as a function of θ, for the beampattern design in Fig. 1.12b with $w_c = 1$ and for $N = 256$. Note that the difference is quite small. We define the mean-squared error (MSE) between the beampatterns obtained by using $\hat{\mathbf{R}}_{xx}$ and $\mathbf{R}$ as the average of the square of (1.98) over all mesh gridpoints and over the set of Monte Carlo trials. The MSE as a function of N, obtained from 1000 Monte Carlo trials, is shown in Fig. 1.13b. As expected, the larger the sample number N, the smaller the MSE.

Next, we examine the MSEs of the location estimates $\{\hat{\theta}_k\}$ obtained by Capon and of the complex amplitude estimates $\{\hat{\beta}_k\}$ obtained by AML (see Ref. 46 or Section 1.4). In particular, we compare the MSEs obtained using the initial omnidirectional probing with those obtained using the optimal beampattern matching design shown in Fig. 1.12 with $\Delta = 5^\circ$ and $w_c = 1$. Figures 1.14a,b show the MSE curves of the location and complex amplitude estimates obtained for the target at -40° from 1000 Monte Carlo trials (results for the other targets are similar). The estimates obtained using the optimal beampattern matching design are much better; the SNR gain over the omnidirectional design is larger than 10 dB.

Now consider an example where two of the targets are closely spaced. We assume that there are $K = 3$ targets, located at $\theta_1 = -40^\circ$, $\theta_2 = 0^\circ$, and $\theta_3 = 3^\circ$ with complex amplitudes equal to $\beta_1 = \beta_2 = \beta_3 = 1$. There is a strong jammer at 25° with an unknown waveform, which is uncorrelated with the transmitted MIMO radar waveforms, and with a power equal to 10^6 (60 dB). Each transmitted signal pulse has $N = 256$ samples. The received signal is corrupted by zero-mean circularly symmetric spatially and temporally white Gaussian noise with variance $\sigma^2 = -10$ dB. Figures 1.15a,b show the Capon spectrum and the GLRT pseudospectrum, respectively, for the initial omnidirectional probing; as can be seen from these figures, the two closely spaced targets cannot be resolved. Using this initial probing result, we derive an optimal beampattern matching design using (1.83) with a mesh grid size of 0.1°, $w_l = 1$, $l = 1, \ldots, L$, and $w_c = 1$. Since the initial probing indicated only two dominant peaks, only the locations of these two peaks

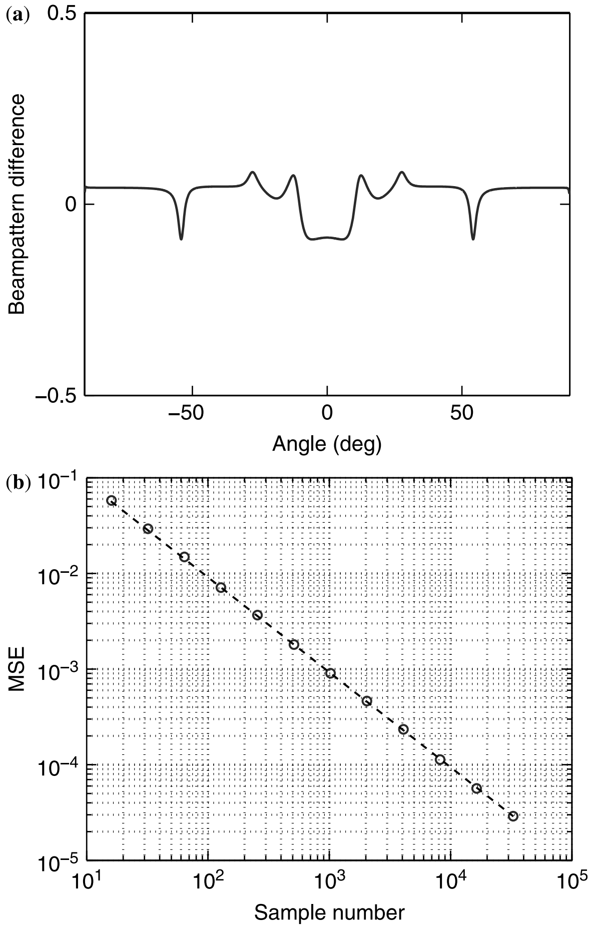

Figure 1.13 Analysis of the beampattern difference resulting from using $\hat{\mathbf{R}}_{xx}$ in lieu of $\mathbf{R}$: (a) beampattern difference versus θ when $N = 256$; (b) average MSE of the beampattern difference as a function of the sample number N.

are used in (1.83). The desired beampattern is given by (1.97) with $\Delta = 10^\circ$ and $\hat{K} = 2$. Figures 1.15c,d, respectively, show the Capon spectrum and the GLRT pseudospectrum for the optimal probing. In principle, the two closely spaced targets are now resolved.

To conclude this section, we consider an example where the desired beampattern has only one wide beam centered at 0° with a width of 60°. Figure 1.16a shows the result for the beampattern matching design in (1.83) with a mesh grid size of 0.1°, $w_l = 1$, $l = 1, \ldots, L$, and $w_c = 0$. Figure 1.16b shows the corresponding phased-array beampattern obtained by using the additional constraint of $\text{rank}(\mathbf{R}) = 1$ in (1.83). We note that, under the elemental power constraint, the number of degrees of freedom (DOF) of the phased array that can be used for beampattern design is

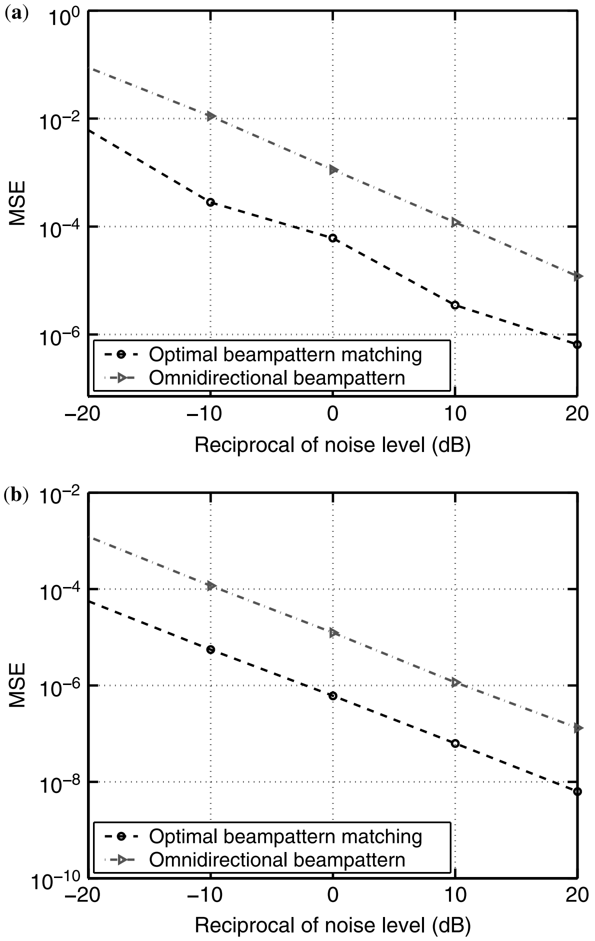

Figure 1.14 MSEs of (a) the location estimates and of (b) the complex amplitude estimates for the first target, as functions of $-10\ \log_{10} \sigma^2$, obtained with initial omnidirectional probing and with probing using the beampattern matching design for $\Delta = 5^\circ$, $w_c = 1$, and $c_p = 1$.

equal to only $M_t - 1$ (real-valued parameters); consequently, it is difficult for the phased array to synthesize a proper wide beam. The MIMO design, however, can be used to achieve a beampattern significantly closer to the desired beampattern because of its much higher DOF value: $M_t^2 - M_t$.

1.6.4.2 Minimum-Sidelobe Beampattern Design Consider the minimum sidelobe beampattern design problem in (1.93), with the mainbeam centered at $\theta_0 = 0^\circ$, with a 3 dB width equal to 20° ($\theta_2 = -\theta_1 = 10^\circ$), and with $c_p = 1$, for the same MIMO radar scenario as the one considered in Fig. 1.11. The sidelobe region is $\Omega = [-90^\circ, -20^\circ] \cup [20^\circ, 90^\circ]$. The MIMO minimum-sidelobe beampattern design is shown in Fig. 1.17a. Note that the peak sidelobe level achieved by the MIMO design is approximately 18 dB below the mainlobe peak level. Figure 1.17b shows the corresponding phased-array beampattern obtained by using the additional constraint $\text{rank}(\mathbf{R}) = 1$. The phased-array design fails to provide a proper mainlobe (it suffers from peak splitting), and its peak sidelobe level is much higher than that of its MIMO counterpart.

Figure 1.18 is similar to Fig. 1.17, except that now we allow the elemental powers to be between 80% and 120% of $c_p/M_t = 1/10$, while the total power is still constrained to be $c_p = 1$. Observe that by allowing such a flexibility in setting the elemental powers, we can bring down the peak sidelobe level of the MIMO beampattern by $\sim$3 dB. The phased-array design, on the other hand, does not appear to improve in any significant way.

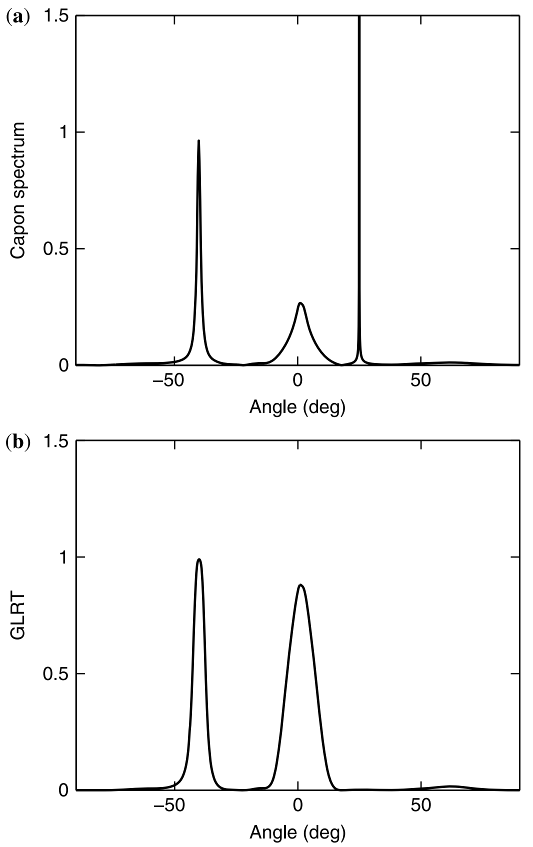

Figure 1.15 The Capon spatial spectra and the GLRT pseudospectra as functions of θ: (a) Capon for initial omnidirectional probing; (b) GLRT for initial omnidirectional probing; (c) Capon for optimal probing; (d) GLRT for optimal probing.

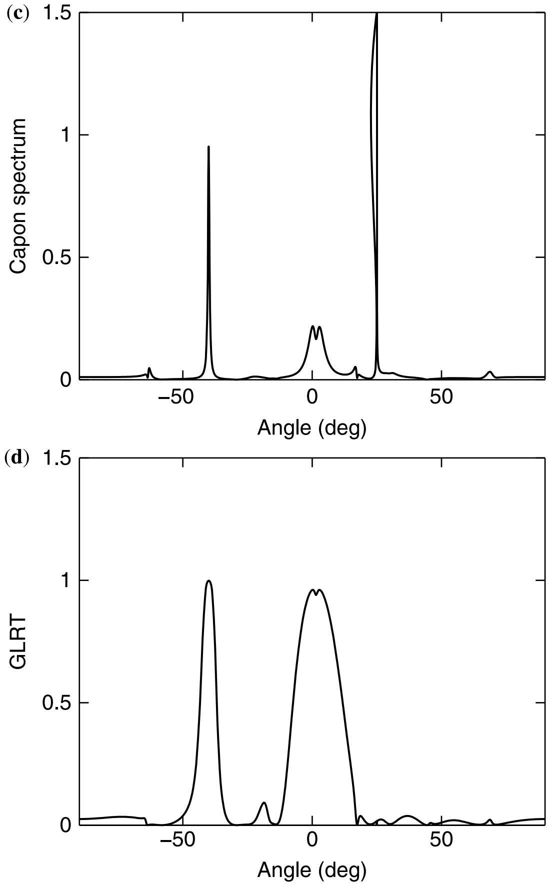

Figure 1.15 *Continued.*

1.6.5 Application to Ultrasound Hyperthermia Treatment of Breast Cancer

Breast cancer is the most common nonskin malignancy in women and the second leading cause of female cancer mortality [60]. There are over 200,000 new cases of invasive breast cancer diagnosed each year in the United States, where one out of every seven women will be diagnosed with breast cancer in her lifetime (the American Cancer Society, 2006, URL: http://www.cancer.org).

The development of breast cancer imaging techniques, such as microwave imaging [61,62], ultrasound imaging [63,64], thermal acoustic imaging [65], and magnetic resonance imaging (MRI), has improved the ability to visualize and accurately locate the breast tumor without the need for surgery [66]. The possibility of noninvasive local hyperthermia treatment of breast cancer is also under investigation. Many studies have been performed to demonstrate the effectiveness of local

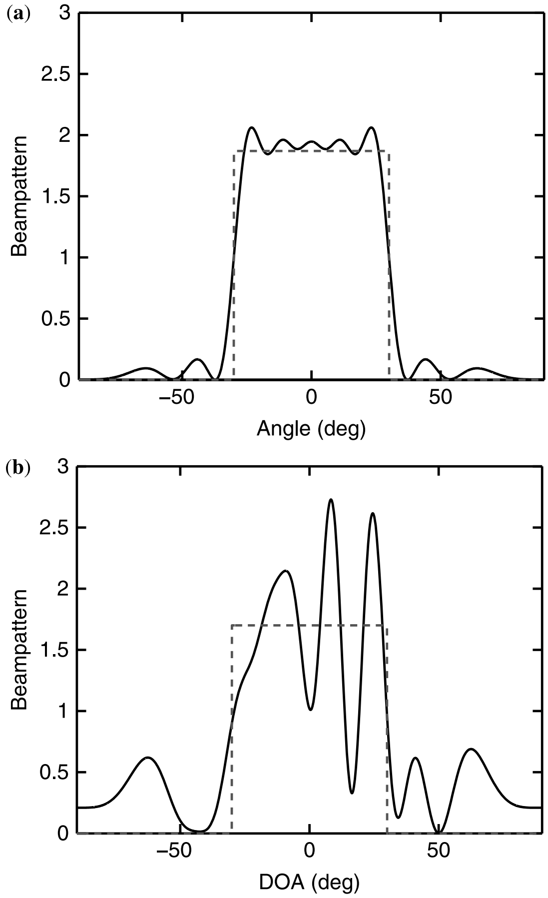

Figure 1.16 Beampattern matching designs under the uniform elemental power constraint: (a) MIMO; (b) phased array.

hyperthermia on the treatment of breast cancer [67,68]. A challenge in the local hyperthermia treatment of breast cancer is to heat the malignant tumors to a temperature above 43°C for ~30–60 min, and at the same time maintain a low temperature level in the surrounding healthy breast tissue region.

There are two major classes of local hyperthermia techniques: microwave hyperthermia [69] and ultrasound hyperthermia [70]. The penetration of microwave in biological tissues is poor. Moreover, the focal spot generated by microwave is undesirable at the normal–cancerous tissues interface because of the long wavelength of the microwave. Ultrasound can achieve much better penetration depths than can microwave. However, because the acoustic wavelength is very short, the focal spot generated by ultrasound is very small (<1 mm in diameter) compared to the large tumor region (centimeters in diameter, on the average). Thus, many focal spots are required for complete tumor coverage, and this results in a long treatment time and missed cancer cells.

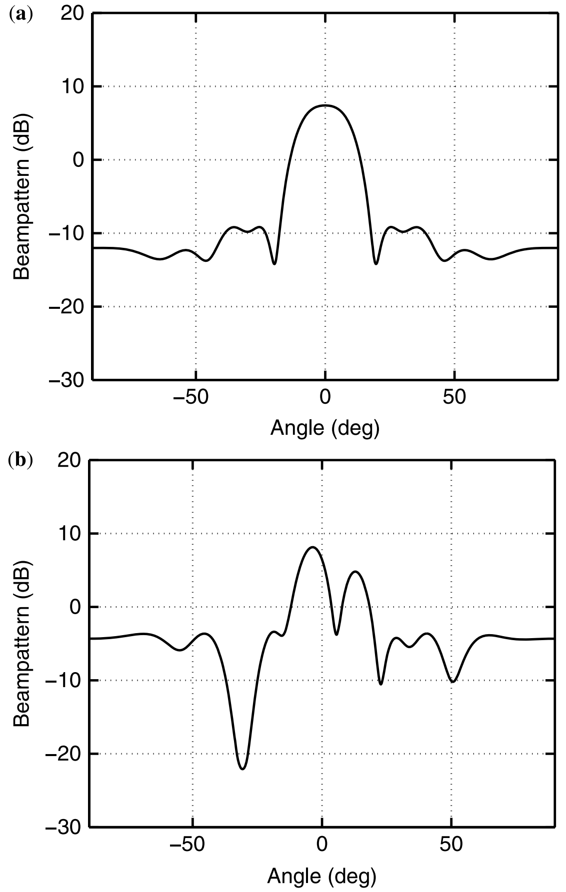

Figure 1.17 Minimum sidelobe beampattern designs, under the uniform elemental power constraint, when the 3 dB mainbeam width is 20°: (a) MIMO; (b) phased array.

We apply below the MIMO (or waveform diversity based) transmit beampattern designs to the ultrasound hyperthermia treatment of breast cancer.

1.6.5.1 Waveform Design We consider an ultrasound hyperthermia system as shown in Fig. 1.19. Let $\mathbf{r}_0$ denote the center location of the tumor, which is assumed to be previously estimated accurately using breast cancer imaging techniques. There are M_t acoustic transducers deployed around the breast at locations $\mathbf{r}_m (m = 1, 2, \ldots, M_t)$. We assume that the transmitted acoustic signals $\{x_m(n)\}$ are narrowband and that each acoustic transducer is omnidirectional. The baseband signal at a location $\mathbf{r}$ inside the breast can be described as

$$y(\mathbf{r}, n) = \sum_{m=1}^{M_t} \frac{e^{-j2\pi f_0 \tau_m(\mathbf{r})}}{\| \mathbf{r}_m - \mathbf{r} \|^{1/2}} x_m(n), \qquad n = 1,\ 2, \ldots, N \tag{1.99}$$

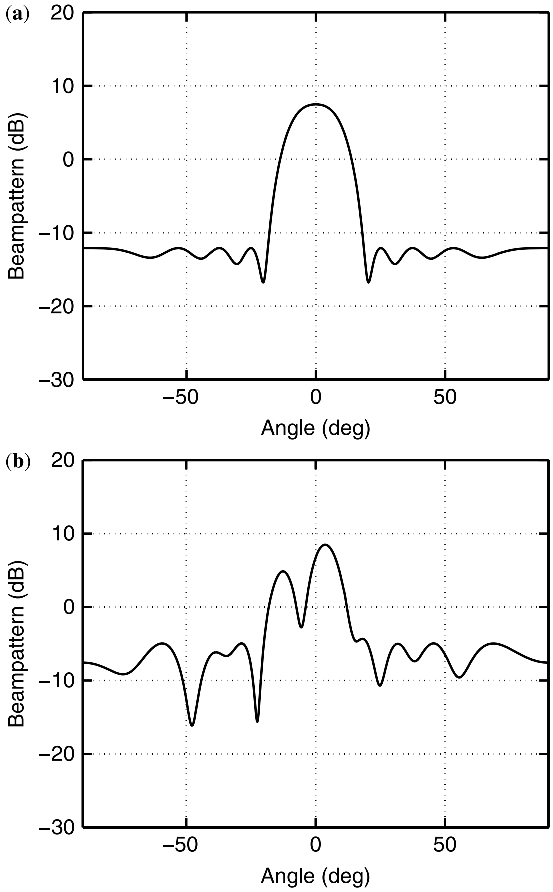

Figure 1.18 Minimum sidelobe beampattern designs, under a relaxed ($\pm 20\%$) elemental power constraint, when the 3 dB mainbeam width is 20°: (a) MIMO; (b) phased array.

where f_0 is the carrier frequency

$$\tau_m(\mathbf{r}) = \frac{\|\mathbf{r}_m - \mathbf{r}\|}{c} \tag{1.100}$$

is the time needed by the signal emitted via the mth transducer to arrive at the location $\mathbf{r}$, where c is the sound speed inside the breast tissues, and $1/(\|\mathbf{r}_m - \mathbf{r}\|^{1/2})$ is the propagation attenuation of the acoustic wave. Therefore the steering vector is

$$\mathbf{a}(\mathbf{r}) = \left[\frac{e^{j2\pi f_0 \tau_1(\mathbf{r})}}{\| \mathbf{r}_1 - \mathbf{r} \|^{1/2}} \quad \frac{e^{j2\pi f_0 \tau_2(\mathbf{r})}}{\| \mathbf{r}_2 - \mathbf{r} \|^{1/2}} \quad \cdots \quad \frac{e^{j2\pi f_0 \tau_{M_t}(\mathbf{r})}}{\| \mathbf{r}_{M_t} - \mathbf{r} \|^{1/2}}\right]^{\mathrm{T}} \tag{1.101}$$

Equation (1.99) can be rewritten as

$$y(\mathbf{r}, n) = \mathbf{a}^*(\mathbf{r})\mathbf{x}(n), \qquad n = 1, 2, \ldots, N \tag{1.102}$$

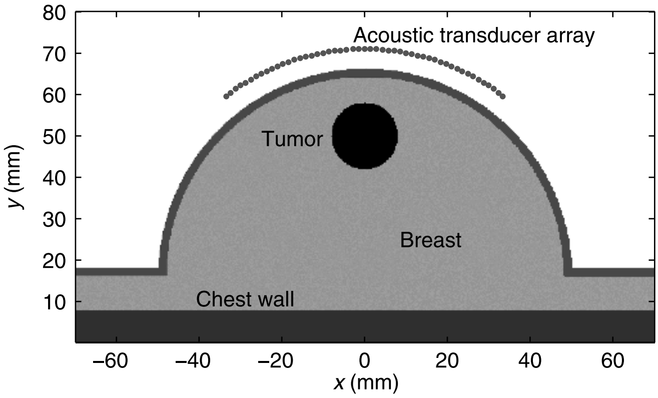

Figure 1.19 Acoustic array and breast model.

The power of the transmitted signals at location **r** (i.e., the transmit beampattern) is given by

$$P(\mathbf{r}) = \mathrm{E}\{y(\mathbf{r}, n)y^*(\mathbf{r}, n)\} = \mathbf{a}^*(\mathbf{r})\mathbf{R}\mathbf{a}(\mathbf{r}) \tag{1.103}$$

The transmit beampattern is a function of the location **r**.

The goal here is to focus the acoustic power onto the entire tumor region while minimizing the peak power level in the surrounding healthy breast tissue region. The corresponding MIMO or waveform diversity-based beampattern design problem is to choose the covariance matrix **R**, under the uniform elemental power constraint [see (1.82)], to achieve the following goals (see Ref. 71 and also (1.93) for a related design problem):

1. Achieve a predetermind main-beam width that is matched to the entire tumor region (be within 10% of the power deposited at the tumor center).
2. Minimize the peak sidelobe level in a prescribed region (the surrounding healthy breast tissue region).

This problem can be formulated as

$$\begin{aligned}
\min_{t,\mathbf{R}} \quad & -t \\
\text{s.t.} \quad & \mathbf{a}^*(\mathbf{r}_0)\mathbf{R}\mathbf{a}(\mathbf{r}_0) - \mathbf{a}^*(\mu)\mathbf{R}\mathbf{a}(\mu) \geq t, \qquad \forall\, \mu \in \Omega_B \\
& \mathbf{a}^*(\nu)\mathbf{R}\mathbf{a}(\nu) \geq 0.9\mathbf{a}^*(\mathbf{r}_0)\mathbf{R}\mathbf{a}(\mathbf{r}_0), \qquad \forall\, \nu \in \Omega_T \\
& \mathbf{a}^*(\nu)\mathbf{R}\mathbf{a}(\nu) \leq 1.1\mathbf{a}^*(\mathbf{r}_0)\mathbf{R}\mathbf{a}(\mathbf{r}_0), \qquad \forall\, \nu \in \Omega_T \\
& \mathbf{R} \geq 0 \\
& R_{mm} = \frac{c_p}{M_t}, \quad m = 1,2, \ldots, M_t,
\end{aligned} \tag{1.104}$$

where Ω_T and Ω_B, which are assumed to be given, denote the tumor region and the surrounding healthy breast tissue region (sidelobe region), respectively.

As shown in Section 1.6.2, this beampattern design problem is a semidefinite program (SDP) that can be efficiently solved in polynomial time using public-domain software. Once $\mathbf{R}$ is determined, a signal sequence $\{\mathbf{x}(n)\}$ that has $\mathbf{R}$ as its covariance matrix can be synthesized as

$$\mathbf{x}(n) = \mathbf{R}^{1/2}\mathbf{w}(n), \qquad n = 1, 2, \ldots, N \tag{1.105}$$

where $\{\mathbf{w}(n)\}$ is a sequence of i.i.d. random vectors with mean zero and covariance matrix $\mathbf{I}$, and $\mathbf{R}^{1/2}$ denotes a Hermitian square root of $\mathbf{R}$.

By transmitting $\mathbf{x}(n)$ given in (1.105) using the acoustic transducer array, we can approximately get a desired high acoustic power deposition in the entire tumor region, and at the same time minimize the power deposition in the surrounding healthy breast tissue region.

1.6.5.2 Simulation Examples For simulation purposes, the 2D breast model shown in Fig. 1.19 is considered. This breast model is a semicircle with a diameter equal to 10 cm, which includes breast tissues, skin, and chest wall. The acoustic properties of the breast tissues are assumed to be random with a variation of $\pm 5\%$ around the nominal values. A tumor with a diameter of 16 mm is embedded below the skin, with the tumor center location at $x = 0$ mm, $y = 50$ mm. There are 51 acoustic transducers deployed uniformly around the breast model. The distance between two adjacent acoustic transducers is 1.5 mm (this is 0.5λ of the carrier frequency, which is equal to 500 kHz).

The two basic linear acoustic wave generation equations are [72,73]

$$\rho \frac{\partial}{\partial t}\mathbf{u}(\mathbf{r}, t) = -\nabla p(\mathbf{r}, t) \tag{1.106}$$

and

$$\nabla \cdot \mathbf{u}(\mathbf{r}, t) = -\frac{1}{\rho c^2}\frac{\partial}{\partial t}p(\mathbf{r}, t) + \alpha p(\mathbf{r}, t) \tag{1.107}$$

where $\mathbf{u}(\mathbf{r}, t)$ is the acoustic velocity vector, $p(\mathbf{r}, t)$ is the acoustic pressure field, ρ is the mass density, $\nabla \cdot \mathbf{u}$ is the divergence of $\mathbf{u}$, and α is the attenuation coefficient. The nominal values of ρ, c, and α for different breast tissues are listed in Table 1.1 [64,74,75]. The values for the tumor are considered to be the same as those for the chest wall, as tumor-specific values are not available in the literature. The finite-difference time-domain (FDTD) approach is used to compute the acoustic field distribution based on Eqs. (1.106) and (1.107). More details about FDTD for acoustic simulations can be found in the literature [76,77].

TABLE 1.1 Typical Acoustic Parameters of Breast Tissue

Tissue	ρ (kg/m^3)	c (m/s)	α (dB/cm)
Breast tissue	1020	1510	0.26
Skin	1100	1537	1.0
Chest wall	1041	1580	0.28
Tumor	1041	1580	0.28

TABLE 1.2 Typical Thermal Parameters of Breast Tissue

Tissue	K [W/(m · °C)]	A (W/m^3)	B [W/(°C · m^3)]	C [J/(kg · °C)]
Breast tissue	0.499	480	2700	3550
Skin	0.376	1620	9100	3500
Chest wall	0.564	480	2700	3510
Tumor	0.564	480	2700	3510

Once the acoustic pressure has been calculated, the acoustic power deposition at location $\mathbf{r}$, denoted as $Q(\mathbf{r})$, is given by [73]

$$Q(\mathbf{r}) = \frac{\alpha}{\rho c} |p(\mathbf{r})|^2 \tag{1.108}$$

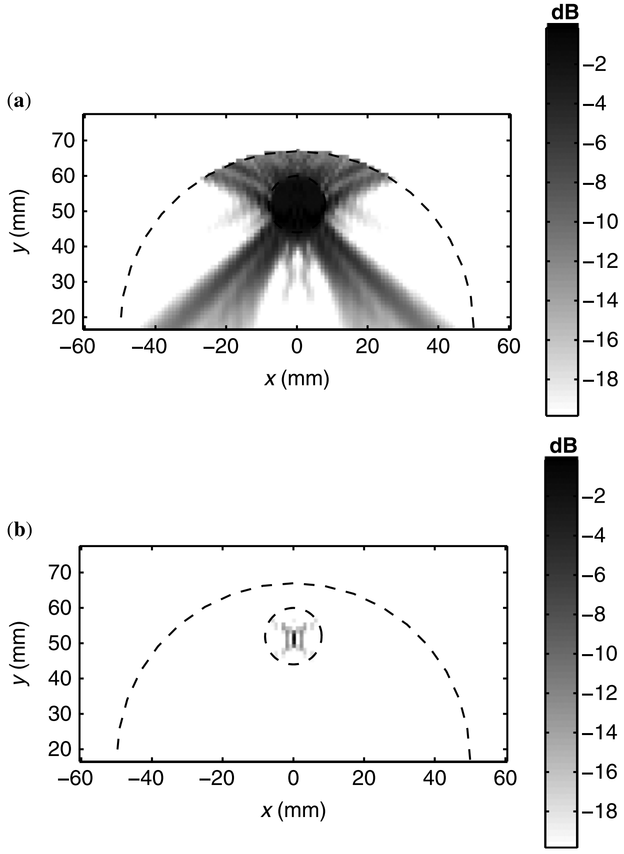

Figure 1.20 Transmit beampatterns $P(\mathbf{r})$ in (1.103) for (a) and in (1.111) for (b): (a) waveform diversity; (b) phased array.

After obtaining the acoustic power deposition, a 2D thermal model is used to calculate the temperature distribution in the breast tissues. The thermal model is based on the bioheat equation [5]

$$\begin{aligned}&\nabla \cdot (K(\mathbf{r})\, \nabla T(\mathbf{r}, t)) + A(\mathbf{r}) + Q(\mathbf{r}) - B(\mathbf{r})(T(\mathbf{r}, t) - T_B)\\&\quad = C(\mathbf{r})\rho(\mathbf{r})\frac{\partial T(\mathbf{r}, t)}{\partial t}\end{aligned} \tag{1.109}$$

where $K(\mathbf{r})$ is the thermal conductivity, $A(\mathbf{r})$ is metabolic heat production, $B(\mathbf{r})$ represents the heat exchange mechanism due to capillary blood perfusion, $C(\mathbf{r})$ is the specific heat, and T_B is the blood temperature, which can be assumed as the body temperature. The thermal parameters used for our breast model are listed in Table 1.2 (more detailed discussions can be found in Ref. 78).

The thermal model is also simulated using the FDTD method [79]. The body temperature and the environmental temperature are set to 36.8°C and 20°C,

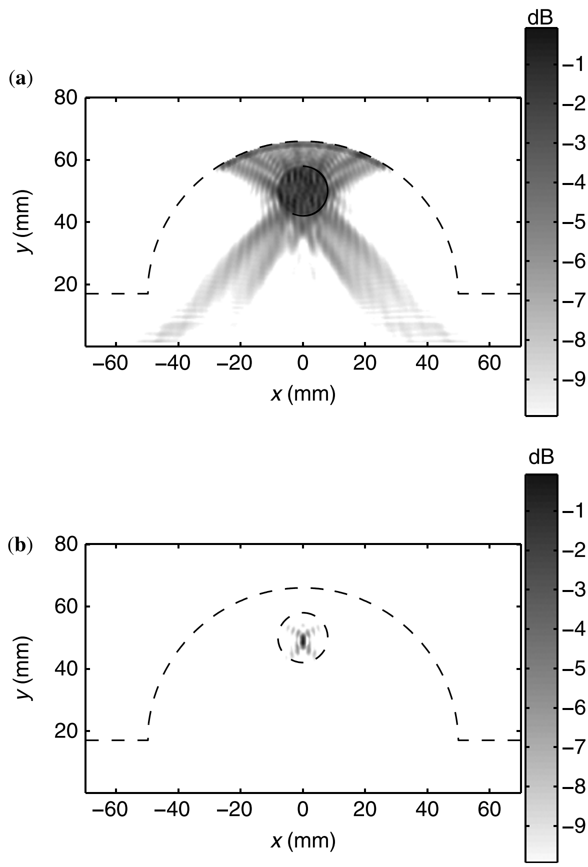

Figure 1.21 FDTD simulated power deposition: (a) waveform diversity; (b) phased array.

respectively. The convective boundary condition is used at the skin surface. We demonstrate the performance of the proposed waveform diversity-based method via several numerical examples. The conventional delay-and-sum (DAS) [i.e., the least-squares (LS) approach in Refs. 27 and 28] phased-array beamforming method is also applied to the same model for comparison purposes. The DAS-based phased-array beamformer transmits a single waveform using the following weight vector:

$$\mathbf{w} = \sqrt{\frac{c_p}{M_t}}\left[e^{j2\pi f_0 \tau_1(\mathbf{r})} \quad e^{j2\pi f_0 \tau_2(\mathbf{r})} \quad \ldots \quad e^{j2\pi f_0 \tau_{M_t}(\mathbf{r})}\right]^T \tag{1.110}$$

The corresponding beampattern is

$$P(\mathbf{r}) = |\mathbf{a}^*(\mathbf{r})\,\mathbf{w}|^2 \tag{1.111}$$

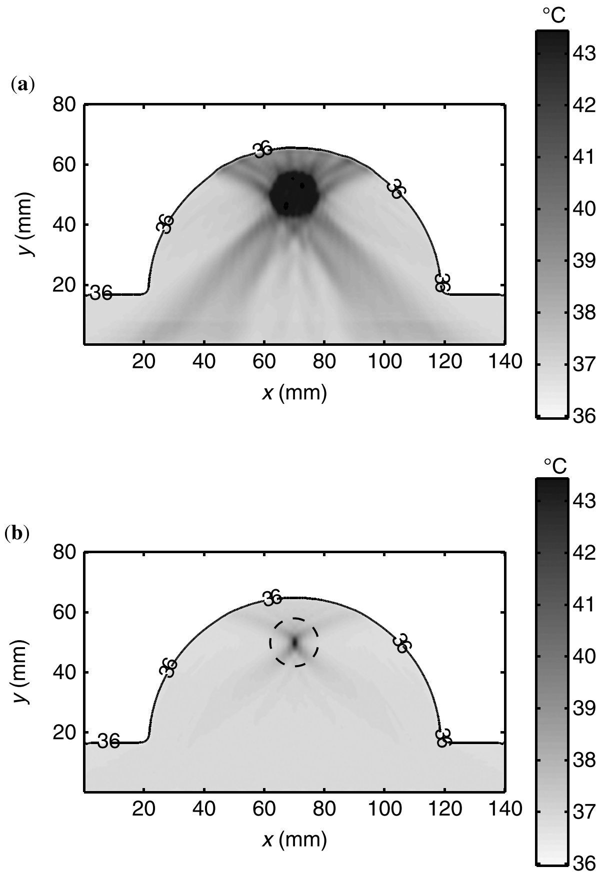

Figure 1.22 Temperature distribution: (a) waveform diversity; (b) phased array.

Figure 1.20 shows the transmit beampatterns within the breast model. Figure 1.20a is the beampattern obtained with the waveform diversity technique, which is calculated by using (1.103) with the optimal covariance matrix $\mathbf{R}$ determined by using (1.104). The figure shows that the mainbeam is matched to the tumor region well, and the sidelobe level is low. Figure 1.20b is the DAS beampattern, which is calculated using (1.111). The DAS beampattern is very narrow, and is focused on the center of the tumor. Figures 1.21a,b show the FDTD simulated acoustic power densities within the breast model for the waveform diversity technique and DAS, respectively. The acoustic power densities in Fig. 1.21 agree well with the beampatterns in Fig. 1.20; the waveform diversity allows the focal spot to be matched to the entire tumor region.

Figure 1.22 shows the temperature distribution within the breast model. Figure 1.22a is the result for waveform diversity, which shows that the entire tumor region is heated to a temperature greater than 43°C while the surrounding healthy tissues have a lower temperature (below 40°C). By comparison, DAS heats only a very small region in the center of the tumor to a temperature greater than 43°C.

1.7 CONCLUSIONS

We have presented some recent results on the emerging technology of MIMO radar with collocated antennas. We have shown that the waveform diversity offered by such a MIMO radar system enables significant superiority over its phased-array counterpart, including improved parameter identifiability, direct applicability of adaptive nonparametric techniques for parameter estimation, enhanced performance of parametric algorithms, as well as superior flexibility of transmit beampattern designs. We hope that this presentation of our results on the MIMO radar, along with the related results presented in the chapters that follow by our colleagues, will stimulate the interest deserved by this topic in both academia and government agencies as well as industry.

For the reader who wants to probe further, we mention here some ongoing research results that have not been included in this chapter. Some initial results on waveform optimization with respect to the covariance matrix of the transmitted waveforms for MIMO spacetime adaptive processing (STAP) have been presented in Refs. 19 and 29. Given a covariance matrix of the transmitted waveforms, obtained in an optimization stage such as the one described in Section 1.6, or in Refs. 19 and 29, or simply prespecified, the problem becomes that of determining a signal waveform matrix whose covariance matrix is equal or close to the given covariance matrix, *and* that also satisfies some practically motivated constraints (such as constant-modulus or low peak-to-average-power ratio constraints). In a previous paper we presented [80] a computationally attractive cyclic optimization algorithm for the synthesis of such a waveform matrix, which (approximately) realizes a given optimal covariance matrix under various practical constraints. For MIMO synthetic aperture radar (SAR) imaging, we presented [81] a related cyclic optimization algorithm for the synthesis of constant-modulus transmit signals with good auto- and cross-correlation properties. In our earlier studies cited among the references for this chapter, we also discussed the use of an instrumental variables approach to design receive filters that can be used to minimize the impact of scatterers in nearby range bins on the received signals from the range bin of interest (the so-called range compression problem).

APPENDIX IA GENERALIZED LIKELIHOOD RATIO TEST

We assume that the columns of the residual term $\mathbf{Z}$ in (1.29) are independently and identically distributed circularly symmetric complex Gaussian random vectors with zero-mean and unknown covariance matrix $\mathbf{Q}$. We derive the GLRT for each θ of interest. For notational brevity, we omit the argument θ of ρ, $\mathbf{a}$, $\mathbf{b}$, and β.

Following Kelly [82] (see also Ref. 83), we define the GLR as follows

$$\rho = 1 - \left[\frac{\max_{\mathbf{Q}} f(\mathbf{Y}|\beta = 0, \mathbf{Q})}{\max_{\beta,\mathbf{Q}} f(\mathbf{Y}|\beta, \mathbf{Q})}\right]^{1/N} \tag{1A.1}$$

where

$$f(\mathbf{Y}|\beta, \mathbf{Q}) = \pi^{-NM_r}|\mathbf{Q}|^{-N}\exp\left\{-\mathrm{tr}[\mathbf{Q}^{-1}(\mathbf{Y} - \mathbf{b}^c\beta\mathbf{a}^*\mathbf{X})(\mathbf{Y} - \mathbf{b}^c\beta\mathbf{a}^*\mathbf{X})^*]\right\} \tag{1A.2}$$

is the probability density function of the observed data matrix $\mathbf{Y}$ given the parameters β and $\mathbf{Q}$, and $\mathrm{tr}(\cdot)$ and $|\cdot|$ denote the trace and determinant of a matrix, respectively. From (1A.1), we note that the value of the GLR, ρ, lies between 0 and 1. If there is a target at a θ of interest, we usually have $\max_{\beta,\mathbf{Q}} f(\mathbf{Y}|\beta, \mathbf{Q}) \gg \max_{\mathbf{Q}} f(\mathbf{Y}|\beta = 0, \mathbf{Q})$ (i.e., $\rho \approx 1$; otherwise $\rho \approx 0$).

Solving the optimization problems in (1A.1) with respect to $\mathbf{Q}$ yields

$$\max_{\mathbf{Q}} f(\mathbf{Y}|\beta = 0, \mathbf{Q}) = (\pi e)^{-NM_r}|\hat{\mathbf{R}}_{yy}|^{-N} \tag{1A.3}$$

and

$$\max_{\beta,\mathbf{Q}} f(\mathbf{Y}|\beta, \mathbf{Q}) = (\pi e)^{-NM_r}\left\{\min_{\beta}\left|\frac{1}{N}(\mathbf{Y} - \mathbf{b}^c\beta\mathbf{a}^*\mathbf{X})(\mathbf{Y} - \mathbf{b}^c\beta\mathbf{a}^*\mathbf{X})^*\right|\right\}^{-N} \tag{1A.4}$$

Applying the technique used in Refs. 40 and 84, we obtain

$$\begin{aligned}
&\left|\frac{1}{N}(\mathbf{Y} - \mathbf{b}^c\beta\mathbf{a}^*\mathbf{X})(\mathbf{Y} - \mathbf{b}^c\beta\mathbf{a}^*\mathbf{X})^*\right| \\
&= \left|\hat{\mathbf{R}}_{yy} - \frac{\mathbf{Y}\mathbf{X}^*\mathbf{a}\beta^*\mathbf{b}^T}{N} - \frac{\mathbf{b}^c\beta\mathbf{a}^*\mathbf{X}\mathbf{Y}^*}{N} + |\beta|^2\mathbf{b}^c\mathbf{a}^*\hat{\mathbf{R}}_{xx}\mathbf{a}\mathbf{b}^T\right| \\
&= \left|\hat{\mathbf{Q}} + (\mathbf{a}^*\hat{\mathbf{R}}_{xx}\mathbf{a})\left(\mathbf{b}^c\beta - \frac{\mathbf{Y}\mathbf{X}^*\mathbf{a}}{N(\mathbf{a}^*\hat{\mathbf{R}}_{xx}\mathbf{a})}\right)\left(\mathbf{b}^c\beta - \frac{\mathbf{Y}\mathbf{X}^*\mathbf{a}}{N(\mathbf{a}^*\hat{\mathbf{R}}_{xx}\mathbf{a})}\right)^*\right|
\end{aligned}$$

$$
\begin{aligned}
&= |\hat{\mathbf{Q}}| \left| \mathbf{I} + (\mathbf{a}^*\hat{\mathbf{R}}_{xx}\mathbf{a})\,\hat{\mathbf{Q}}^{-1}\left(\mathbf{b}^c\beta - \frac{\mathbf{Y}\mathbf{X}^*\mathbf{a}}{N(\mathbf{a}^*\hat{\mathbf{R}}_{xx}\mathbf{a})}\right)\left(\mathbf{b}^c\beta - \frac{\mathbf{Y}\mathbf{X}^*\mathbf{a}}{N(\mathbf{a}^*\hat{\mathbf{R}}_{xx}\mathbf{a})}\right)^* \right| \\
&= |\hat{\mathbf{Q}}| \left[1 + (\mathbf{a}^*\hat{\mathbf{R}}_{xx}\mathbf{a})\left(\mathbf{b}^c\beta - \frac{\mathbf{Y}\mathbf{X}^*\mathbf{a}}{N(\mathbf{a}^*\hat{\mathbf{R}}_{xx}\mathbf{a})}\right)^* \hat{\mathbf{Q}}^{-1}\left(\mathbf{b}^c\beta - \frac{\mathbf{Y}\mathbf{X}^*\mathbf{a}}{N(\mathbf{a}^*\hat{\mathbf{R}}_{xx}\mathbf{a})}\right) \right] \\
&\geq |\hat{\mathbf{Q}}| \left[1 + \frac{\mathbf{a}^*\mathbf{X}\mathbf{Y}^*}{N^2(\mathbf{a}^*\hat{\mathbf{R}}_{xx}\mathbf{a})}\hat{\mathbf{Q}}^{-1}\left(\mathbf{I} - \frac{\mathbf{b}^c\mathbf{b}^T\hat{\mathbf{Q}}^{-1}}{\mathbf{b}^T\hat{\mathbf{Q}}^{-1}\mathbf{b}^c}\right)\mathbf{Y}\mathbf{X}^*\mathbf{a} \right]
\end{aligned}
\tag{1A.5}
$$

where we have applied the fact that $|\mathbf{I} + \mathbf{A}_1\mathbf{B}_1| = |\mathbf{I} + \mathbf{B}_1\mathbf{A}_1|$ [31], and the equality holds when $\beta = \hat{\beta}_{\text{APES}}$. Note that

$$
\begin{aligned}
&|\hat{\mathbf{Q}}| \left[1 + \frac{\mathbf{a}^*\mathbf{X}\mathbf{Y}^*}{N^2(\mathbf{a}^*\hat{\mathbf{R}}_{xx}\mathbf{a})}\hat{\mathbf{Q}}^{-1}\left(\mathbf{I} - \frac{\mathbf{b}^c\mathbf{b}^T\hat{\mathbf{Q}}^{-1}}{\mathbf{b}^T\hat{\mathbf{Q}}^{-1}\mathbf{b}^c}\right)\mathbf{Y}\mathbf{X}^*\mathbf{a} \right] \\
&= |\hat{\mathbf{Q}}| \left| \mathbf{I} + \hat{\mathbf{Q}}^{-1}\left(\mathbf{I} - \frac{\mathbf{b}^c\mathbf{b}^T\hat{\mathbf{Q}}^{-1}}{\mathbf{b}^T\hat{\mathbf{Q}}^{-1}\mathbf{b}^c}\right)\frac{\mathbf{Y}\mathbf{X}^*\mathbf{a}\mathbf{a}^*\mathbf{X}\mathbf{Y}^*}{N^2(\mathbf{a}^*\hat{\mathbf{R}}_{xx}\mathbf{a})} \right| \\
&= \left| \hat{\mathbf{Q}} + \left(\mathbf{I} - \frac{\mathbf{b}^c\mathbf{b}^T\hat{\mathbf{Q}}^{-1}}{\mathbf{b}^T\hat{\mathbf{Q}}^{-1}\mathbf{b}^c}\right)\frac{\mathbf{Y}\mathbf{X}^*\mathbf{a}\mathbf{a}^*\mathbf{X}\mathbf{Y}^*}{N^2(\mathbf{a}^*\hat{\mathbf{R}}_{xx}\mathbf{a})} \right| \\
&= \left| \hat{\mathbf{R}}_{yy} - \frac{\mathbf{b}^c\mathbf{b}^T\hat{\mathbf{Q}}^{-1}\mathbf{Y}\mathbf{X}^*\mathbf{a}\mathbf{a}^*\mathbf{X}\mathbf{Y}^*}{N^2(\mathbf{b}^T\hat{\mathbf{Q}}^{-1}\mathbf{b}^c)(\mathbf{a}^*\hat{\mathbf{R}}_{xx}\mathbf{a})} \right| \\
&= |\hat{\mathbf{R}}_{yy}| \left| \mathbf{I} - \frac{\hat{\mathbf{R}}_{yy}^{-1}\mathbf{b}^c\mathbf{b}^T\hat{\mathbf{Q}}^{-1}\mathbf{Y}\mathbf{X}^*\mathbf{a}\mathbf{a}^*\mathbf{X}\mathbf{Y}^*}{N^2(\mathbf{b}^T\hat{\mathbf{Q}}^{-1}\mathbf{b}^c)(\mathbf{a}^*\hat{\mathbf{R}}_{xx}\mathbf{a})} \right| \\
&= |\hat{\mathbf{R}}_{yy}| \left[1 - \frac{\mathbf{b}^T\hat{\mathbf{Q}}^{-1}(\hat{\mathbf{R}}_{yy} - \hat{\mathbf{Q}})\hat{\mathbf{R}}_{yy}^{-1}\mathbf{b}^c}{\mathbf{b}^T\hat{\mathbf{Q}}^{-1}\mathbf{b}^c} \right] \\
&= |\hat{\mathbf{R}}_{yy}| \; \frac{\mathbf{b}^T\hat{\mathbf{R}}_{yy}^{-1}\mathbf{b}^c}{\mathbf{b}^T\hat{\mathbf{Q}}^{-1}\mathbf{b}^c}
\end{aligned}
\tag{1A.6}
$$

where again we have utilized the fact that $|\mathbf{I} + \mathbf{A}_1\mathbf{B}_1| = |\mathbf{I} + \mathbf{B}_1\mathbf{A}_1|$.

From (1A.5) and (1A.6), it follows that

$$
\min_{\beta} \left| \frac{1}{N}(\mathbf{Y} - \mathbf{b}^c\beta\mathbf{a}^*\mathbf{X})(\mathbf{Y} - \mathbf{b}^c\beta\mathbf{a}^*\mathbf{X})^* \right| = |\hat{\mathbf{R}}_{yy}| \; \frac{\mathbf{b}^T\hat{\mathbf{R}}_{yy}^{-1}\mathbf{b}^c}{\mathbf{b}^T\hat{\mathbf{Q}}^{-1}\mathbf{b}^c} \tag{1A.7}
$$

By using (1A.3), (1A.4), and (1A.7) in (1A.1), we see that the GLR in (1.61) follows immediately.

APPENDIX 1B LEMMA AND PROOF

Lemma 1B.1 Let $\mathbf{R} \in \mathcal{C}^{M_t \times M_t}$, and let $\tilde{\mathbf{R}} \in \mathcal{R}^{2M_t \times 2M_t}$ be as defined in (1.96). Then

$$\operatorname{rank}(\mathbf{R}) = M_t - m \Longleftrightarrow \operatorname{rank}(\tilde{\mathbf{R}}) = 2(M_t - m) \quad \text{for} \quad m = 0, \ldots, M_t \tag{1B.1}$$

***Proof*:** Let $\mathbf{v} \in \mathcal{C}^{M_t \times 1}$, $\mathbf{v} \neq 0$, be a vector in the null space of $\mathbf{R}$, $\mathcal{N}(\mathbf{R})$:

$$\mathbf{R}\mathbf{v} = 0 \tag{1B.2}$$

This implies that

$$\tilde{\mathbf{R}} \begin{bmatrix} \operatorname{Re}\{\mathbf{v}\} \\ \operatorname{Im}\{\mathbf{v}\} \end{bmatrix} = 0 \tag{1B.3}$$

Moreover, since (1B.2) also implies $\mathrm{R}(j\mathbf{v}) = 0$, we must also have

$$\tilde{\mathbf{R}} \begin{bmatrix} -\operatorname{Im}\{\mathbf{v}\} \\ \operatorname{Re}\{\mathbf{v}\} \end{bmatrix} = 0 \tag{1B.4}$$

The vectors appearing in (1B.3) and (1B.4) are linearly independent of each other. Indeed, if we assume that they were not, then there would exist a nonzero complex-valued scalar, say, $\zeta \neq 0$, such that

$$\begin{bmatrix} \operatorname{Re}\{\mathbf{v}\} & -\operatorname{Im}\{\mathbf{v}\} \\ \operatorname{Im}\{\mathbf{v}\} & \operatorname{Re}\{\mathbf{v}\} \end{bmatrix} \begin{bmatrix} \operatorname{Re}\{\zeta\} \\ \operatorname{Im}\{\zeta\} \end{bmatrix} = 0 \implies \mathbf{v}\ \zeta = 0 \implies \mathbf{v} = 0 \tag{1B.5}$$

which contradicts the assumption that $\mathbf{v} \neq 0$.

Thus, we have shown that from each $\mathbf{v} \in \mathcal{N}(\mathbf{R})$ we can obtain [as in (1B.3) and (1B.4)] two linearly independent vectors in $\mathcal{N}(\tilde{\mathbf{R}})$. Furthermore, we can use an argument similar to (1B.5) to show that if the vectors $\mathbf{v}_1, \mathbf{v}_2, \ldots, \in \mathcal{N}(\mathbf{R})$ are linearly independent, then so are the corresponding vectors in $\mathcal{N}(\tilde{\mathbf{R}})$. It follows from these observations that

$$\operatorname{rank}(\mathbf{R}) = M_t - m \implies \operatorname{rank}(\tilde{\mathbf{R}}) \leq 2(M_t - m), \quad m \in [0, M_t] \tag{1B.6}$$

Conversely, for each $\boldsymbol{\nu} \neq 0$ satisfying $\tilde{\mathbf{R}}\boldsymbol{\nu} = 0$ [i.e., $\boldsymbol{\nu} \in \mathcal{N}(\tilde{\mathbf{R}})$], we can write $\boldsymbol{\nu}$ as $[\operatorname{Re}\{\mathbf{v}^T\} \quad \operatorname{Im}\{\mathbf{v}^T\}]^T$, and therefore we can build a $\mathbf{v}$ such that $\mathbf{v} \in \mathcal{N}(\mathbf{R})$. Furthermore, owing the structure of $\tilde{\mathbf{R}}$, it follows, as above, that also $[-\operatorname{Im}\{\mathbf{v}^T\} \ \operatorname{Re}\{\mathbf{v}^T\}]^T \in \mathcal{N}(\tilde{\mathbf{R}}))$, and that $[\operatorname{Re}\{\mathbf{v}^T\} \quad \operatorname{Im}\{\mathbf{v}^T\}]^T$ and $[-\operatorname{Im}\{\mathbf{v}^T\} \quad \operatorname{Re}\{\mathbf{v}^T\}]^T$ are linearly independent of each other. Therefore, for any two such linearly independent vectors in $\mathcal{N}(\tilde{\mathbf{R}})$, there is one vector $\mathbf{v} \in \mathcal{N}(\mathbf{R})$. Again, similar to what was shown above, the linear independence of the vectors in $\mathcal{N}(\tilde{\mathbf{R}})$ implies that of the corresponding vectors in $\mathcal{N}(\mathbf{R})$. Therefore, we have shown that

$$\operatorname{rank}(\tilde{\mathbf{R}}) = 2(M_t - m) \implies \operatorname{rank}(\mathbf{R}) \leq M_t - m, \quad m \in [0, M_t] \tag{1B.7}$$

The result stated in (1B.1) follows from (1B.6) and (1B.7). Indeed, if $\text{rank}(\mathbf{R}) = M_t - m$, then we must have $\text{rank}(\tilde{\mathbf{R}}) = 2(M_t - m)$ [otherwise (1B.6) and (1B.7) would imply that $\text{rank}(\tilde{\mathbf{R}}) < 2(M_t - m)$, by (1B.6), and thus that $\text{rank}(\mathbf{R}) < M_t - m$, by (1B.7), which is a contradiction]. Similarly, (1B.6) and (1B.7) can be used to conclude that $\text{rank}(\tilde{\mathbf{R}}) = 2(M_t - m) \implies \text{rank}(\mathbf{R}) = M_t - m$. □

Lemma 1B.1 is related to a number of results reported by Goodman [85] for matrices of the form of (1.96), but it does not appear in that cited paper. In fact, while the result from Lemma 1B.1 may possibly be known, we have not been able to locate it in the literature, and this is why we provided a proof for it in this appendix.

ACKNOWLEDGMENTS

This work was supported in part by the Office of Naval Research under Grant N00014-0710293, the National Science Foundation under Grant CCF-0634786, the Defense Advanced Research Projects Agency under Grant HR0011-06-1-0031, and the Swedish Science Council (VR). Opinions, interpretations, conclusions, and recommendations are those of the authors and are not necessarily endorsed by the United States government. We are also grateful to Dr. Luzhou Xu, Ms. Yao Xie, Mr. William Roberts, Dr. Bin Guo, Dr. Xiayu Zheng, and Ms. Xumin Zhu for their contributions to the research results reported herein and for their help with putting this chapter together.

REFERENCES

1. E. Fishler, A. Haimovich, R. Blum, D. Chizhik, L. Cimini, and R. Valenzuela, MIMO radar: An idea whose time has come, *Proc. IEEE Radar Conf.* April 2004, pp. 71–78.
2. E. Fishler, A. Haimovich, R. Blum, L. Cimini, D. Chizhik, and R. Valenzuela, Performance of MIMO radar systems: Advantages of angular diversity, *Proc. 38th Asilomar Conf. Signals, Systems and Computers*, Pacific Grove, CA, Nov. 2004, Vol. 1, pp. 305–309.
3. E. Fishler, A. Haimovich, R. Blum, L. Cimini, D. Chizhik, and R. Valenzuela, Spatial diversity in radars — models and detection performance, *IEEE Trans. Signal Process.* **54**(3):823–838 (March 2006).
4. Y. Yang and R. S. Blum, MIMO radar waveform design based on mutual information and minimum mean-square error estimation, *IEEE Trans. Aerospace Electron. Syst.* **43**(1):330–343 (Jan. 2007).
5. T. Aittomaki and V. Koivunen, Low-complexity method for transmit beamforming in MIMO radars, *Proc. 2007 IEEE Int. Conf. Acoustics, Speech, and Signal Processing*, Honolulu, April 2007.
6. I. Bekkerman and J. Tabrikian, Spatially coded signal model for active arrays, *Proc. 2004 IEEE Int. Conf. Acoustics, Speech, and Signal Processing*, Montreal, Quebec, Canada, March 2004, Vol. 2, pp. ii/209–ii/212.
7. I. Bekkerman and J. Tabrikian, Target detection and localization using MIMO radars and sonars, *IEEE Trans. Signal Process.* **54**:3873–3883 (Oct. 2006).

8. I. Bekkerman and J. Tabrikian, Space-time coding for active arrays, *IEEE Trans. Signal Process.* (in press).
9. D. W. Bliss and K. W. Forsythe, Multiple-input multiple-output (MIMO) radar and imaging: Degrees of freedom and resolution, *Proc. 37th Asilomar Conf. Signals, Systems and Computers*, Pacific Grove, CA, Nov. 2003, Vol. 1, pp. 54–59.
10. K. W. Forsythe and D. W. Bliss, Waveform correlation and optimization issues for MIMO radar, *Proc. 39th Asilomar Conf. Signals, Systems and Computers*, Pacific Grove, CA, Nov. 2005, pp. 1306–1310.
11. K. W. Forsythe, D. W. Bliss, and G. S. Fawcett, Multiple-input multiple-output (MIMO) radar: Performance issues, *Proc. 38th Asilomar Conf. Signals, Systems and Computers*, Pacific Grove, CA, Nov. 2004, Vol. 1, pp. 310–315.
12. D. R. Fuhrmann and G. San Antonio, Transmit beamforming for MIMO radar systems using partial signal correlations, *Proc. 38th Asilomar Conf. Signals, Systems and Computers*, Pacific Grove, CA, Nov. 2004, Vol. 1, pp. 295–299.
13. D. R. Fuhrmann and G. San Antonio, Transmit beamforming for MIMO radar systems using signal cross-correlation, *IEEE Trans. Aerospace Electron. Syst.* (in press).
14. N. Lehmann, E. Fishler, A. M. Haimovich, R. S. Blum, D. Chizhik, L. Cimini, and R. Valenzuela, Evaluation of transmit diversity in MIMO-radar direction finding, *IEEE Trans. Signal Process.* **55**(5):2215–2225 (May 2007).
15. J. Li and P. Stoica, MIMO radar — diversity means superiority, *Proc. 14th Annual Workshop on Adaptive Sensor Array Processing* (invited), MIT Lincoln Laboratory, Lexington, MA, June 2006.
16. J. Li and P. Stoica, MIMO radar with collocated antennas: Review of some recent work, *IEEE Signal Process. Mag.* **24**(5):106–114 (Sept. 2007).
17. J. Li, P. Stoica, and Y. Xie, On probing signal design for MIMO radar, *Proc. 40th Asilomar Conf. Signals, Systems and Computers* (invited), Pacific Grove, CA, Oct. 2006.
18. J. Li, P. Stoica, L. Xu, and W. Roberts, On parameter identifiability of MIMO radar, *IEEE Signal Process. Lett.* **14**(12):968–971 (Dec. 2007).
19. J. Li, L. Xu, P. Stoica, K. W. Forsythe, and D. W. Bliss, Range compression and waveform optimization for MIMO radar: A Cramér-Rao bound based study, *IEEE Trans. Signal Process.* **56**(1):218–232 (Jan. 2008).
20. V. F. Mecca, D. Ramakrishnan, and J. L. Krolik, MIMO radar space-time adaptive processing for multipath clutter mitigation, *Proc. 4th IEEE Workshop on Sensor Array and Multichannel Processing*, Waltham, MA, July 2006.
21. D. J. Rabideau and P. Parker, Ubiquitous MIMO multifunction digital array radar, *Proc. 37th Asilomar Conf. Signals, Systems and Computers*, Pacific Grove, CA, Nov. 2003.
22. F. C. Robey, S. Coutts, D. Weikle, J. C. McHarg, and K. Cuomo, MIMO radar theory and exprimental results, *Proc. 38th Asilomar Conf. Signals, Systems and Computers*, Pacific Grove, CA, Nov. 2004, Vol. 1, pp. 300–304.
23. P. Stoica, J. Li, and Y. Xie, On probing signal design for MIMO radar, *IEEE Trans. Signal Process.* **55**(8):4151–4161 (Aug. 2007).
24. J. Tabrikian, Barankin bounds for target localization by MIMO radars, *Proc. 4th IEEE Workshop on Sensor Array and Multi-channel Processing*, Waltham, MA, July 2006.

25. J. Tabrikian and I. Bekkerman, Transmission diversity smoothing for multi-target localization, *Proc. 2005 IEEE Int. Conf. Acoustics, Speech, and Signal Processing*, Philadelphia, PA, March 2005, Vol. 4, pp. iv/1041–iv/1044.
26. L. Xu, J. Li, and P. Stoica, Target detection and parameter estimation for MIMO radar systems, *IEEE Trans. Aerospace Electron. Syst.* (in press).
27. L. Xu, J. Li, and P. Stoica, Adaptive techniques for MIMO radar, *Proc. 4th IEEE Workshop on Sensor Array and Multi-channel Processing*, Waltham, MA, July 2006.
28. L. Xu, J. Li, and P. Stoica, Radar imaging via adaptive MIMO techniques, *Proc. 14th European Signal Processing Conf.* (invited), Florence, Italy, Sept. 2006.
29. L. Xu, J. Li, P. Stoica, K. W. Forsythe, and D. W. Bliss, Waveform optimization for MIMO radar: A Cramer-Rao bound based study, *Proc. 2007 IEEE Int. Conf. Acoustics, Speech, and Signal Processing*, Honolulu, April 2007.
30. L. Xu and J. Li, Iterative generalized likelihood ratio test for MIMO radar, *IEEE Trans. Signal Process.* **55**(6):2375–2385, (June 2007).
31. P. Stoica and R. L. Moses, *Spectral Analysis of Signals*, Prentice-Hall, Upper Saddle River, NJ, 2005.
32. H. L. Van Trees, *Optimum Array Processing: Part IV of Detection, Estimation, and Modulation Theory*, Wiley, New York, 2002.
33. A. Nehorai, D. Starer, and P. Stoica, Direction-of-arrival estimation in applications with multipath and few snapshots, *Circuits Syst. Signal Process.* **10**:327–342 (1991).
34. M. Wax and I. Ziskind, On unique localization of multiple sources by passive sensor arrays, *IEEE Trans. Acoust. Speech Signal Process.* **37**(7):996–1000 (July 1989).
35. J. R. Guerci, *Space-Time Adaptive Processing for Radar*, Artech House, Norwood, MA, 2003.
36. R. Klemm, *Principles of Space-Time Adaptive Processing*, IEE Press, London, 2002.
37. J. Ward, *Space-Time Adaptive Processing for Airborne Radar*, Technical Report 1015, MIT Lincoln Laboratory, Dec. 1994.
38. D. J. Rabideau and A. O. Steinhardt, Improved adaptive clutter cancellation through data-adaptive training, *IEEE Trans. Aerospace Electron. Syst.* **35**(3):879–891 (July 1999).
39. J. Capon, High resolution frequency-wavenumber spectrum analysis, *Proc. IEEE* **57**:1408–1418 (Aug. 1969).
40. J. Li and P. Stoica, An adaptive filtering approach to spectral estimation and SAR imaging, *IEEE Trans. Signal Process.* **44**(6):1469–1484 (June 1996).
41. P. Stoica, H. Li, and J. Li, A new derivation of the APES filter, *IEEE Signal Process. Lett.* **6**(8):205–206 (Aug. 1999).
42. E. G. Larsson, J. Li, and P. Stoica, High-resolution nonparametric spectral analysis: Theory and applications, in *High-Resolution and Robust Signal Processing*, Y. Hua, A. B. Gershman, and Q. Cheng (eds.), Marcel-Dekker, New York, 2003, pp. 151–251.
43. P. Stoica, A. Jakobsson, and J. Li, Capon, APES and matched-filterbank spectral estimation, *Signal Process.* **66**(1):45–59 (April 1998).
44. H. Li, J. Li, and P. Stoica, Performance analysis of forward-backward matched-filterbank spectral estimators, *IEEE Trans. Signal Process.* **46**:1954–1966 (July 1998).
45. A. Jakobsson and P. Stoica, Combining Capon and APES for estimation of spectral lines, *Circuits Syst. Signal Process.* **19**(2):159–169 (2000).

46. L. Xu, P. Stoica, and J. Li, A diagonal growth curve model and some signal processing applications, *IEEE Trans. Signal Process.* **54**(9):3363–3371 (Sept. 2006).
47. D. A. Harville, *Matrix Algebra from a Statistician's Perspective*, Springer, New York, 1997.
48. K. M. Buckley and L. J. Griffiths, An adaptive generalized sidelobe canceller with derivative constraints, *IEEE Trans. Anten. Propag.* **34**:311–319 (March 1986).
49. J. Li, P. Stoica, and Z. Wang, On robust Capon beamforming and diagonal loading, *IEEE Trans. Signal Process.* **51**(7):1702–1715 (July 2003).
50. P. Stoica, Z. Wang, and J. Li, Robust Capon beamforming, *IEEE Signal Process. Lett.* **10**(6):172–175 (June 2003).
51. J. Li and P. Stoica (eds.), *Robust Adaptive Beamforming*, Wiley, Hoboken, NJ, 2005.
52. T. L. Marzetta, A new interpretation for Capon's maximum likelihood method of frequency-wavenumber spectrum estimation, *IEEE Trans. Acoust. Speech Signal Process.* **31**(2):445–449 (April 1983).
53. J. Li, P. Stoica, and Z. Wang, Doubly constrained robust Capon beamformer, *IEEE Trans. Signal Process.* **52**(9):2407–2423 (Sept. 2004).
54. P. Stoica and G. Ganesan, Maximum-SNR spatial-temporal formatting for MIMO channels, *IEEE Trans. Signal Process.* **50**(12):3036–3042 (Dec. 2002).
55. P. Stoica and Y. Selen, Model-order selection: A review of information criterion rules, *IEEE Signal Process. Mag.* **21**(4):36–47 (July 2004).
56. J. Li and P. Stoica, Efficient mixed-spectrum estimation with applications to target feature extraction, *IEEE Trans. Signal Process.* **44**:281–295 (Feb. 1996).
57. J. F. Sturm, Using SeDuMi 1.02, a MATLAB toolbox for optimization over symmetric cones, *Optim. Meth. Software Online* **11–12**:625–653 (Oct. 1999) (available at http://www2.unimaas.nl/sturm/software/sedumi.html).
58. S. Boyd and L. Vandenberghe, *Convex Optimization*, Cambridge Univ. Press, UK, 2004.
59. R. Orsi, U. Helmke, and J. B. Moore, A Newton-like method for solving rank constrained linear matrix inequalities, *Proc. 43rd IEEE Conf. Decision and Control*, 2004, pp. 3138–3144.
60. E. C. Fear, P. M. Meaney, and M. A. Stuchly, Microwaves for breast cancer detection, *IEEE Potentials* **22**(1):12–18 (Feb.–March 2003).
61. B. Guo, Y. Wang, J. Li, P. Stoica, and R. Wu, Microwave imaging via adaptive beamforming methods for breast cancer detection, *J. Electromagn. Waves Appl.* **20**(1):53–63 (2006).
62. P. M. Meaney, M. W. Fanning, D. Li, S. P. Poplack, and K. D. Paulsen, A clinical prototype for active microwave imaging of the breast, *IEEE Trans. Microwave Theory Tech.* **48**(11):1841–1853 (Nov 2000).
63. F. W. Kremkau, *Diagnostic Ultrasound: Principles and Instruments*, Saunders, Philadelphia, PA, 1993.
64. T. Szabo, *Diagnostic Ultrasound Imaging: Inside Out*, Elsevier Academic Press, Burlington, MA, 2004.
65. R. A. Kruger, K. K. Kopecky, A. M. Aisen, D. R. Reinecke, G. A. Kruger, and W. L. Kiser, Thermoacoustic CT with radio waves: A medical imaging paradigm, *Radiology* **211**(1):275–278 (April 1999).
66. D. Gianfelice, A. Khiat, M. Amara, A. Belblidia, and Y. Boulanger, MR imaging-guided focused US ablation of breast cancer: Histopathologic assessment of effectiveness-initial experience, *Radiology* **227**:849–855 (April 2003).

67. M. H. Falk and R. D. Issels, Hyperthermia in oncology, *Int. J. Hypertherm.* **17**(1):1–18 (Jan. 2001).
68. C. C. Vernon, J. W. Hand, S. B. Field, D. Machin, J. B. Whaley, J. Van Der Zee, W. L. J. Van Putten, G. C. Van Rhoon, J. D. P. Van Dijk, D. G. González, F. Liu, P. Goodman, and M. Sherar, Radiotherapy with or without hyperthermia in the treatment of superficial localized breast cancer: Results from five randomized controlled trials, *Int. J. Radiation Oncol. Biol. Phys.* **35**(4):731–744 (July 1996).
69. A. J. Fenn, V. Sathiaseelan, G. A. King, and P. R. Stauffer, Improved localization of energy deposition in adaptive phased-array hyperthermia treatment of cancer, *Lincoln Lab. J.* **9**(2):187–195 (1996).
70. C. J. Diederich and K. Hynynen, Ultrasound technology for hyperthermia, *Ultrasound Med. Biol.* **25**(6):871–887 (July 1999).
71. B. Guo and J. Li, Waveform diversity based ultrasound system for hyperthermia treatment of breast cancer, *IEEE Trans. Biomed. Eng.* **55**(2):822–826 (Feb. 2008).
72. D. T. Blackstock, *Fundamentals of Physical Acoustics*, Wiley, New York, 2000.
73. A. D. Pierce, *Acoustics: An Introduction to Its Physical Principles and Applications*, McGraw-Hill, New York, 1994.
74. F. A. Duck, *Physical Properties of Tissue*, Academic Press, London, 1990.
75. F. A. Duck, A. C. Baker, and H. C. Starritt, *Ultrasound in Medicine*, Institute of Physics Publishing, Bristol, Philadelphia, PA, 1998.
76. T. K. Katsibas and C. S. Antonopoulos, A general form of perfectly matched layers for three-dimensional problems of acoustic scattering in lossless and lossy fluid media, *IEEE Trans. Ultrason. Ferroelectrics Freq. Control* **51**(8):964–972 (Aug. 2004).
77. X. Yuan, D. Borup, J. Wiskin, M. Berggren, and S. A. Johnson, Simulation of acoustic wave propagation in dispersive media with relaxation losses by using FDTD method with PML absorbing boundary condition, *IEEE Trans. Ultrason. Ferroelectrics Freq. Control* **46**(1):14–23 (Jan. 1999).
78. P. Bernardi, M. Cavagnaro, S. Pisa, and E. Piuzzi, Specific absorption rate and temperature elevation in a subject exposed in the far-field of radio-frequency sources operating in the 10-900-MHz range, *IEEE Trans. Biomed. Eng.* **50**(3):295–304 (March 2003).
79. J. Wang and O. Fujiwara, FDTD computation of temperature rise in the human head for portable telephones, *IEEE Trans. Microwave Theory Tech.* **47**(8):1528–1534 (Aug. 1999).
80. P. Stoica, J. Li, X. Zhu, and B. Guo, Waveform synthesis for diversity-based transmit beampattern design, *Proc. 14th IEEE Workshop on Statistical Signal Processing* (invited), Madison, WI, Aug. 2007.
81. J. Li, X. Zheng, and P. Stoica, MIMO SAR imaging: Signal synthesis and receiver design, *Proc. 2nd Int. Workshop on Computational Advances in Multi-Sensor Adaptive Processing* (invited), St. Thomas, US Virgin Islands, 2007.
82. E. J. Kelly, An adaptive detection algorithm, *IEEE Trans. Aerospace Electron. Syst.* **22**(1):115–127 (March 1986).
83. A. Dogandžić and A. Nehorai, Generalized multivariate analysis of variance, *IEEE Signal Process. Mag.* 39–54 (Sept. 2003).
84. Y. Jiang, P. Stoica, and J. Li, Array signal processing in the known waveform and steering vector case, *IEEE Trans. Signal Process.* **52**(1):23–35 (Jan. 2004).
85. N. R. Goodman, Statistical analysis based on a certain multi-variate complex Gaussian distribution, *Ann. Math. Stat.* **34**:152–177 (March 1963).